BRL R 1957

BRL

REPORT NO. 1957

PRELIMINARY COMPUTER COMPUTATIONS FOR SLENDER ROD IMPACT PROBLEMS

V. B. Kucher

February 1977

USA BALLISTIC RESEARCH LABORATORY
ABERDEEN PROVING GROUND, MARYLAND

REPORT DOCUMENTATION PAGE	**READ INSTRUCTIONS BEFORE COMPLETING FORM**
1. REPORT NUMBER BRL Report No. 1957	2. GOVT ACCESSION NO.
	3. RECIPIENT'S CATALOG NUMBER
4. TITLE (*and Subtitle*) Preliminary Computer Computations for Slender Rod Impact Problems	5. TYPE OF REPORT & PERIOD COVERED
	6. PERFORMING ORG. REPORT NUMBER
7. AUTHOR(*s*) V. B. Kucher	8. CONTRACT OR GRANT NUMBER(*s*)
9. PERFORMING ORGANIZATION NAME AND ADDRESS US Army Ballistic Research Laboratory Aberdeen Proving Ground, Maryland 21005	10. PROGRAM ELEMENT, PROJECT, TASK AREA & WORK UNIT NUMBERS 1W161102AH43
11. CONTROLLING OFFICE NAME AND ADDRESS US Army Materiel Development & Readiness Command 5001 Eisenhower Avenue Alexandria, VA 22333	12. REPORT DATE FEBRUARY 1977
	13. NUMBER OF PAGES 61
14. MONITORING AGENCY NAME & ADDRESS(*if different from Controlling Office*)	15. SECURITY CLASS. (*of this report*) Unclassified
	15a. DECLASSIFICATION/DOWNGRADING SCHEDULE

16. DISTRIBUTION STATEMENT (*of this Report*)

Approved for public release; distribution unlimited.

17. DISTRIBUTION STATEMENT (*of the abstract entered in Block 20, if different from Report*)

18. SUPPLEMENTARY NOTES

19. KEY WORDS (*Continue on reverse side if necessary and identify by block number*)

Penetration Mechanics
Hypervelocity Impact
Hydrodynamic Computer Code
Two-dimensional Computer Code
Eulerian Computer Code

20. ABSTRACT (*Continue on reverse side if necessary and identify by block number*)

If the problem of a long slender rod, impacting normally on a thick target, were to be solved on a computer by using a hydrodynamic code, it would soon be discovered that, because of computer memory limitations, the computational cells which describe the rod in the radial direction cannot be as plentiful as one would prefer for details in the penetration phenomena. Three computer runs were made using 2, 4, and 6 radial cells to describe a rod of 1 mm radius. Penetration, target hole growth, pressure and particle velocity histories, and

DD FORM 1 JAN 73 1473 EDITION OF 1 NOV 65 IS OBSOLETE shock wave propagation for these three cases were compared. Based on accuracy and the cost of the computer runs, it was found that the case which used four radial cells provided the most satisfactory tradeoff.

TABLE OF CONTENTS

This page Left Intentionally Blank

LIST OF ILLUSTRATIONS

LIST OF ILLUSTRATIONS

I. INTRODUCTION

Hydrodynamic computer codes have been used for many years to study the phenomena associated with the hypervelocity impact of a projectile on a target. If a code uses cylindrical coordinates for normal impact, the projectile can have various shapes (spheres, cones, right circular cylinders, etc.) that can be easily inputed into a code. Also, the target can have many configurations, the most common being an infinite plate, a circular plate, a semi-infinite solid, and a semi-infinite cicular solid. As long as a characteristic diameter of a projectile is not too small compared to the thickness of a plate or the depth of penetration to be studied, the problem can be set up on a time-tested code and run on a computer without too many preliminary check-out runs. If one considers the problem of a long, slender rod impacting normally on a target when the diameter of the rod is much less than the depth of penetration to be studied, questions arise as to how the projectile-target configuration can be described in the code.

As an input, the code requires information on the outline of the configuration on a grid forming computational cells. The amount of memory of a particular computer limits the number of cells; consequently, if a large number of cells were used to describe a slender rod radially, and the number of cells in the axial direction were fixed, relatively few cells would remain for describing the target radially beyond the rod. Also, it should be noted that as the number of cells that are used in a problem is increased, the running time, and thus the cost of running a problem on a computer, increases.

Can we describe a slender rod radially by 6, 4, or as few as 2 cells without the code generating unacceptable information on penetration rate, target hole growth, shock wave propagation, and pressure fields? As a numerical experiment, the radial dimension of the slender rod was described by 2, 4, and 6 cells and the corresponding problems or computer runs were named R2, R4, and R6, respectively.

II. COMPUTER CODE

The DORF9 code[1] was used in this study. It is a two-dimensional, multimaterial, continuous, Eulerian, hydrodynamic code coupled with a elastic-plastic strength model. An option of Cartesian (x,y) or cylindrically symmetric (r,z) coordinates is available in the code. Also, tracer particles can be used to provide a Lagrangian look to the plotted output.

---

[1] W. E. Johnson, *"Development and Application of Computer Programs Related to Hypervelocity Impact," Systems, Science and Software, 3SR-749, AD 889143, July 1971.*

III. PROJECTILE-TARGET CONFIGURATION

The same projectile-target configuration was used for R2, R4, and R6. The projectile was a copper, semi-infinite rod with a radius of 1.0 mm; the target was a steel, semi-infinite solid. The stationary target was impacted, normally, by a uniform-velocity rod at 7.0 km/s.

IV. ONE-DIMENSIONAL THEORY

Some preliminary calculations are necessary as an aid in establishing the grid size, the description of the projectile and target in terms of cell size, and the expected pressures and particle and shock velocities for comparison with the computer results.

Using Tillotson's equation of state[2] for copper and iron, we find that the rod-target interface region is shocked to a pressure of 0.27 TPa (2.7 Mb) and that the particle velocity in this region is 3.65 km/s.

From one-dimensional shock wave theory, we find that, in laboratory coordinates, a transmitted shock wave propagates into the target at 9.38 km/s and that another shock wave (reflective) propagates in the other direction, away from the target's surface, at 2.05 km/s. The material between these shock waves moves with a particle velocity of 3.65 km/s. If the real time of penetration is limited to 3 μs, the former shock wave would move 28 mm into the target; the latter, 6 mm away from the target into the rod. However, these conditions will prevail in the interface region along the axis of symmetry of the configuration only until a rarefaction wave arrives at the axis of symmetry at about 0.117 μs after impact. This wave, traveling radially at 8.5 km/s from the periphery of the rod, offers a relief to the pressure. The shock wave that is traveling in the rod is choked-off and eventually dissipates. Thus, we would not expect the shock, moving into the rod, to reach a distance of 6 mm from the target's original surface.

From the jet penetration equations[3], which were developed from Bernouilli's incompressible flow, energy equation, we find the interface velocity to be 3.61 km/s and the pressure to be 0.512 Mb or 51.2 GPa. These conditions are for steady-state flow and hence should be good approximations as soon as the Hugoniot pressures are relieved by rarefactions (see above). If the duration of penetration is limited to 3 μs, a rod length of 10.2 mm will be required to supply rod material

---

[2] J. H. Tillotson, "*Metallic Equations of State for Hypervelocity Impact*," *Gulf General Atomic*, GA-3216, *July 1971*.

[3] E. M. Pugh, R. J. Eichelberger, and N. Rostoker, "*Theory of Jet Formation with Lined Conical Cavities*," *Journal of Applied Physics*, *May 1952*.

over this period and a target depth of at least 10.8 mm for target penetration will be required.

V. COMPUTATIONAL GRID

The computational grid is laid out to cover the cross-sectional region of interest of the rod-target configuration with the rod's center-line coinciding with the z-axis. The rod will move in the positive z-direction. The bottom of the grid is transmittive, allowing rod material to be fed into the grid, thus simulating a semi-infinite rod. Initially, based on preliminary estimates and on the guess that numerical noise, traveling down the rod, would not reach the bottom boundary and thus disturb the boundary condition there, 21 mm of rod length were included in the grid. The target occupied the remainder of the grid above the rod. A target depth of 37 mm was selected. Since the top and right boundaries can be selected to be transmittive, allowing material to flow through these boundaries, the target is simulated to be a semi-infinite solid.

Since the radius of the rod was 1.0 mm, the width, Δr, of the cells in the region of the rod was taken as 0.50, 0.250, and 0.1666670 mm for R2, R4, and R6, respectively.

The length, Δz, of the cells in the region of impact was taken to be equal to the Δr's in the corresponding computer runs. The region containing constant or equal Δr's and Δz's was 5 mm from the axis of symmetry in the r-direction and between 20 and 28 mm on the grid in the z-direction. The main comparisons of R2, R4, and R6 will be made in this region for a period of 1 μs.

The right side of Figures 1, 2, and 3 show the computational grids for R2, R4, and R6, respectively. The overall physical dimensions of each of the three grids was 20 mm by 48 mm. The outline of the rod-target configuration is shown with the z-axis as the center-line of the configuration. Notice that a variable grid is used above, below, and to the right of the region consisting of square cells. The variable grid region acts as a shock resevoir, that is, a region where a shock can propagate without leaving the grid (thus eliminating numerical noise from being reflected from the boundaries), but where some information can be gained on the propagating shock wave.

The cells within the outline of the rod were given the following initial conditions:

1. Pressure = 0.0 Pa.
2. Density = 8.9 Mg/m^3.
3. Radial velocity = 0.0 km/s.
4. Axial velocity = 7.0 km/s.
5. Specific internal energy = 0.0 J/g.

Similar initial conditions were given to the target region except that the density was 7.86 Mg/m^3 and the axial velocity was zero.

VI. OPERATIONAL DATA

R2, R4, and R6 were run on the high-speed digital computer, BRLESC2. which is located at the Ballistic Research Laboratories. A summary of the grid characteristics is shown in Table 1, where IMAX is the number of cells or columns in the r-direction, and JMAX is the number of cells or rows in the z-direction. The total number of cells in the grid is the product (IMAX)(JMAX).

Table 1

Problem	IMAX	JMAX	(IMAX)(JMAX)
R2	16	30	480
R4	28	50	1400
R6	39	68	2652

The three problems were run on the computer for a real time of 3 μs. Computer output was printed at 0.0, 0.25, and 0.5 μs (real time) and, thereafter, at 0.5 μs intervals, to and including 3 μs. A summary of the data associated with running the three problems is listed in Table 2.

Table 2

Problem	Computational Time, min	Output, lines
R2	20	726
R4	75	1536
R6	185	2658

The trends from Table 2 are shown in Figures 4 and 5. As the total number of cells in a grid increases, the running time increases and the printed output increases. Also of importance is the fact that the output is also dumped on magnetic tape for plotting and restart purposes, and the larger number of cells in a grid requires the use of more tape.

Usually, at the beginning of a run, all the cells in the grid are not used in the computations since some of the cells are inactive, that is, the velocity is zero in these cells. As the problem runs, the code allows the active grid to grow to the point where eventually all the cells in the grid will be used in the computations.

Figure 6 shows, for R2, R4, and R6, how the number of cells, involved in the computations, grows as the problem progresses cycle by cycle. The curves terminate at the cycle that is equivalent to a real time of 3 μs.

The relationship between real time and cycle number is shown in Figure 7. After an initial interval of running time, the curves are linear. The change in the time between each cycle is determined by the code according to Courant's stability condition where the change in time, for a given stability factor and local sound speed, is directly proportional to the minimum dimension of the cells in the active grid. Thus, the real time per cycle for R2 is twice that of R4 and three times that of R6. The initial nonlinearity of the curves is due to the fact that the stability factor is set, as an initial condition, at a value lower than 0.4, which is the normal running stability factor. The code gradually increases the stability factor to 0.4 as the computations progress.

VII. COMPUTER RESULTS

A. Pressure

Two views of pressure fields at various times are shown in Figures 8 through 23 for R2, R4, and R6. Figures 8, 10, 12, 14, 16, 18, 20, and 22 show the pressure fields as viewed from the target; Figures 9, 11, 13, 15, 17, 19, 21, and 23, as viewed from the rod. These two perspectives allow one to view more readily the pressure fields within the target and rod, respectively. In these figures, the x-coordinate represents the radial coordinate, r, and the y-coordinate represents the axial coordinate, z. The tracer particle outlines of the rod and the front face of the target are shown in the spatial plane of each plot.

With Eulerian codes, the shock front is usually spread over 4 or 5 cells. Consequently, the smaller the dimensions of a cell, the smaller the physical spread of the shock front. However, by decreasing the dimensions of a cell, we increase the running time and the computer memory requirement.

Although the main results of R2, R4, and R6 are being compared for only 1 μs after which time the shock front moves into the variable grid, from a visual inspection of the pressure fields, we observe that the R4 and R6 results have a close resemblence throughout a 3-μs period.

Figures 24, 25, and 26 show the pressure profiles for R2, R4, and R6 along the z-coordinate axis (the axis of symmetry) for the first ¼ μs of real time, which brackets the 0.117-μs time when the rarefaction wave from the projectile's free surface reaches the axis of symmetry. Every cycle is plotted for R2 and R4; the even cycles are plotted for R6. The initial rod-target interface is at z = 21 mm, and a transmitted shock wave and a reflected shock wave move away from this point. R2, R4, and R6 overshootthe 0.27-TPa or 2.7-Mb peak pressure predicted by one-dimensional shock wave theory. R4 and R6 develop a "plateau" region which decays with time. After the peak pressure has been attained, the rod and target free surfaces provide a pressure release, causing the pressure to drop.

Figures 27 through 29 are continuations of the pressure profile graphs (Figures 24 through 26); however, they cover a time period from ¼ to 1 μs. The left side of the graphs shows a rarefaction wave moving in the direction of the rod's motion; the right side, a shock wave moving into the target. These profiles are referenced to the 51.2-GPa or 0.512-Mb pressure (dashed line) which was determined from jet penetration theory.

In general, the R6 pressure envelope is higher than that for R4, and the pressure envelope is higher for R4 than R2. The pressure envelopes for R4 and R6 have a close resemblance (see Figures 24 through 29).

The pressure profile curves, Figures 24 through 29, were used to provide data for the position history of the 40-GPa or 0.4-Mb pressure points (0-¼ μs time period) and 20-GPa or 0.2-Mb pressure points (¼ to 1 μs time period) on these curves. These two pressures were selected arbitrarily. This data was plotted in Figure 30. The upper set of curves provide a history of the shock wave transmitted into the target. The predicted shock wave velocity for early times is shown by the slope of the line. The lower set of curves provides a history of the shock wave reflected into the rod. The predicted shock wave velocity for early times is shown by the slope of the line. This wave moves down the rod for about 0.18 μs and then becomes a rarefaction wave moving in the same direction as the rod. The R4 and R6 curves normally are the closest together.

Figures 31, 32, and 33 show the radial movement and decay of the shock wave during the first microsecond at a constant distance from the surface of the target. Because the cell size is different for R2, R4, and R6, and since the pressure is calculated for the center of each cell, the constant z-coordinates for these pressure profiles is 0.075 mm into the target for R2 and R6 and 0.0625 mm for R4. These z-coordinates correspond to 2, 3, and 5 cells from the target's surface for R2, R4, and R6, respectively. The profiles for R4 and R6 appear to be more similar with one another than with the profiles for R2.

B. Velocity

Velocity fields at various times are shown in Figures 34 through 40 for R2, R4, and R6. The tracer particle outlines of the projectile and the front face of the target are also shown. These figures give an indication of the direction and magnitude of material flow. A vector emanates from the center of each cell that contains material. Some vectors are shown to be outside the projectile-target outline where, normally, the material in these cells has a low density. The DORF9 code does not use tracer particles to control the flow of material at the free surfaces.

Figures 41, 42, and 43 show the particle velocity profiles for R2, R4, and R6 along the z-coordinate axis for the first ¼ μs of real time. Figures 44, 45, and 46 are a continuation of these figures covering a time period from ¼ to 1 μs. These figures correspond to Figures 24 through 29 for the pressure profiles. Every cycle was plotted for R2 and R4; the even cycles were plotted for R6. The initial projectile-target interface was at z = 21 mm. As in the case of the pressure profiles, the particle velocity profiles can be used to obtain data on wave motion similar to that shown in Figure 30.

C. Particle Motion

The DORF9 code has an option for incorporating tracer particles into its computations. These computations are passive in that the Eulerian solution to a problem is not affected by these additional computations. The motion of a particle is determined by the weighted velocities from the cell containing the particle and from neighboring cells.

A group of particles was initially positioned along the axis of symmetry at equal increments with one particle positioned at the projectile-target interface (z = 21 mm). Figures 47, 49, and 51 show the time displacement of these particles along the axis of symmetry for R2, R4, and R6, respectively. The data for these trajectories were obtained from each computational cycle.

The positions of the particles above the interface in the target region remain stationary until the arrival of the shock wave from the interface; then, these particles are set into motion. A dashed curve connects the coordinates where this occurs. The slope of this curve is the shock velocity of the shock wave propagating into the target. Notice that the break in the curves is more definable at positions were the grid was uniform in the z-direction.

The positions of the particles below the interface in the projectile moved at a uniform velocity (the initial velocity of the projectile) until the shock wave that started down the projectile caused a velocity change. The break in these curves is also outlined by a dashed curve which shows that the wave initially moves against the motion of the projectile and then turns, as a rarefaction wave, in the direction that the projectile was initially moving. Notice that this shock never moved downward more than 1 mm from the initial position of the interface. This will be useful information in setting up grids for future problems.

The transmitted and reflected shock wave motions, as determined previously from one-dimensional shock wave theory, are shown for early times. These figures illustrate a method of obtaining wave motion information in addition to the method used in Figure 30.

Figures 48, 50, and 52 depict the interface motion or penetration along the axis of symmetry. These curves were extracted from Figures 47, 49, and 51. At any particular time, the depth of penetration, in order of decreasing magnitudes, is R2, R4, and R6 with R6 being in close agreement with R4.

Particle velocity-time and particle velocity-position information is depicted in Figures 53 through 64. These figures correspond to the position-time figures (Figures 48 through 52). The interface velocity, shown in Figures 58, 60, and 62, are referenced to the velocity previously determined from jet penetration theory.

During the first microsecond of penetration, there is good agreement between R4 and R6 in these velocity profile figures. The "steady-state" penetration velocity is about 3.42 km/s, which is lower than the 3.61 km/s calculated previously from jet penetration theory.

D. Hole Size

Penetration (hole depth) and penetration rate (rate of hole depth) have already been compared and the results for R4 and R6 were found to be in agreement. A comparison of the hole radius at the original surface of the target is shown in Figure 65. These data were obtained by measuring the tracer outlines in Figures 34 through 40. At a given time, the R2 hole radius was larger than that for R4; the R4 hole radius was larger than that for R6.

VIII. CONCLUSION

A comparison of the pressure fields, pressure profiles, velocity profiles, penetration history, hole size, and shock and rarefaction wave propagation indicates that, for the three cases that were run on the computer, the best agreement exists between R4 and R6. The inference is that if a case, "R8", were run, then R6 and R8 would show the best agreement. However, since the running time for each problem increases as the cell size becomes smaller, a tradeoff must be made between "accuracy" and economy. In the case of the three problems which were run, R4 provides the best available tradeoff.

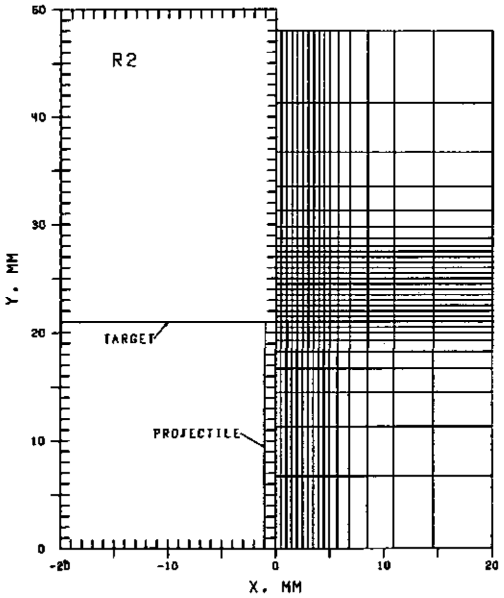

FIGURE 1. R2 GRID CONFIGURATION

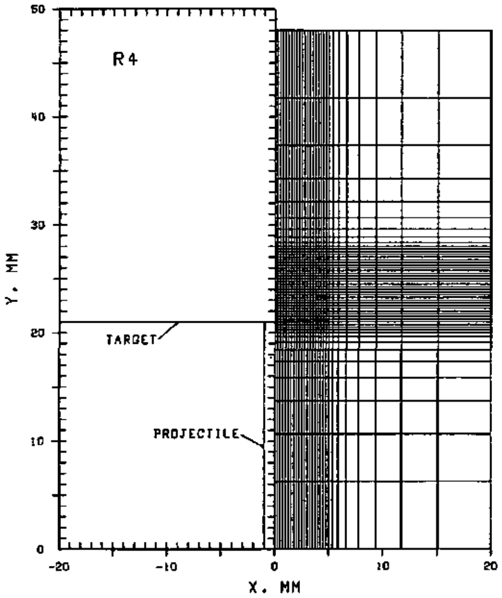

FIGURE 2. R4 GRID CONFIGURATION

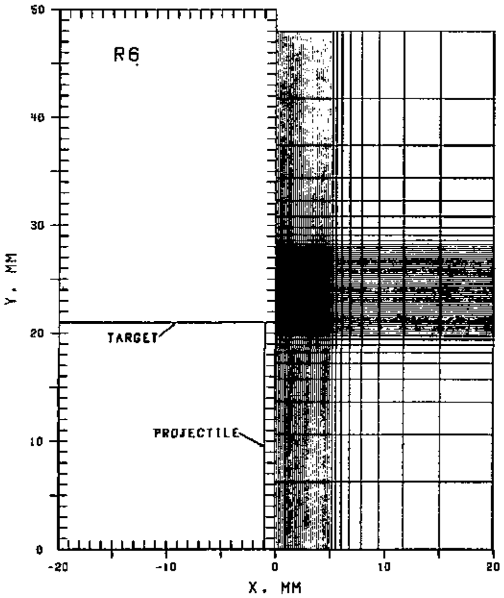

FIGURE 3. R6 GRID CONFIGURATION

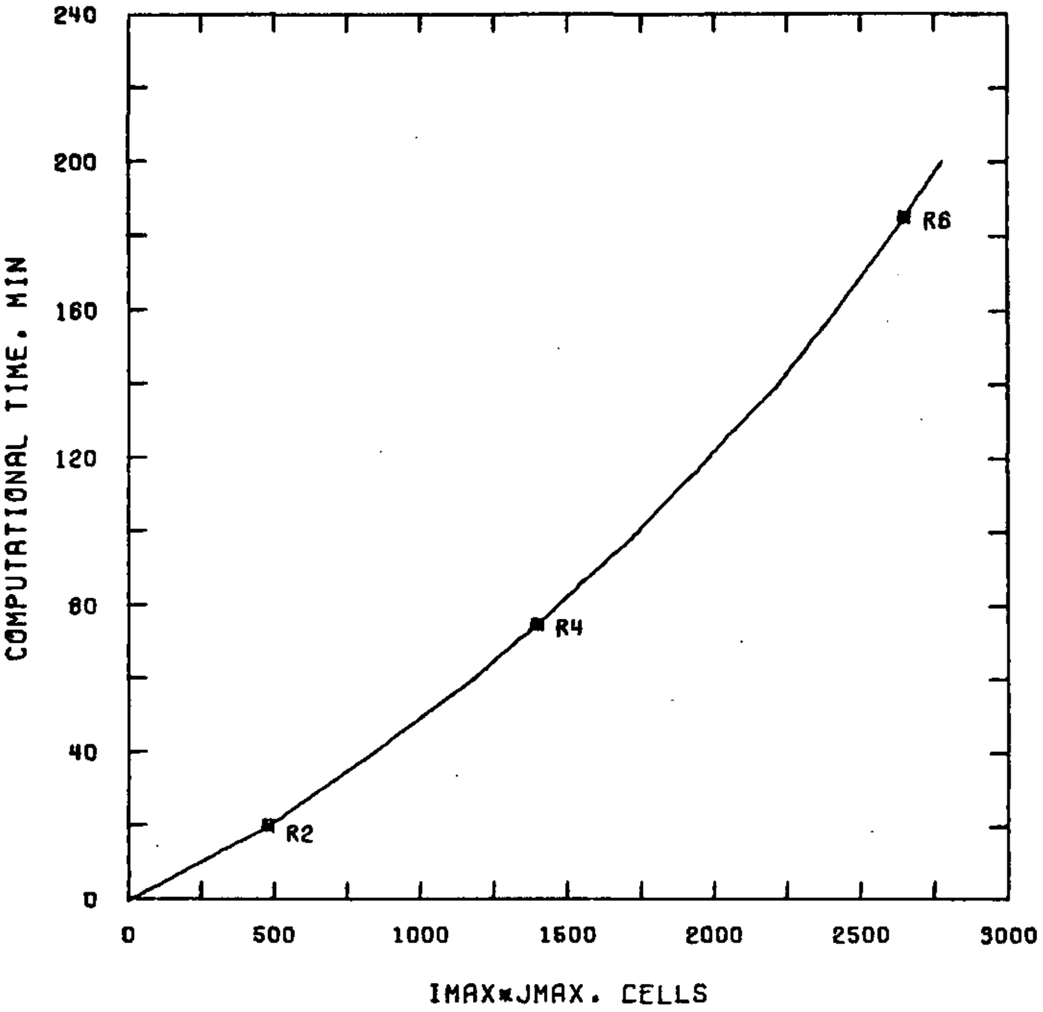

Figure 4. Relation Between Computational Time and the Total Number of Cells in the Grid

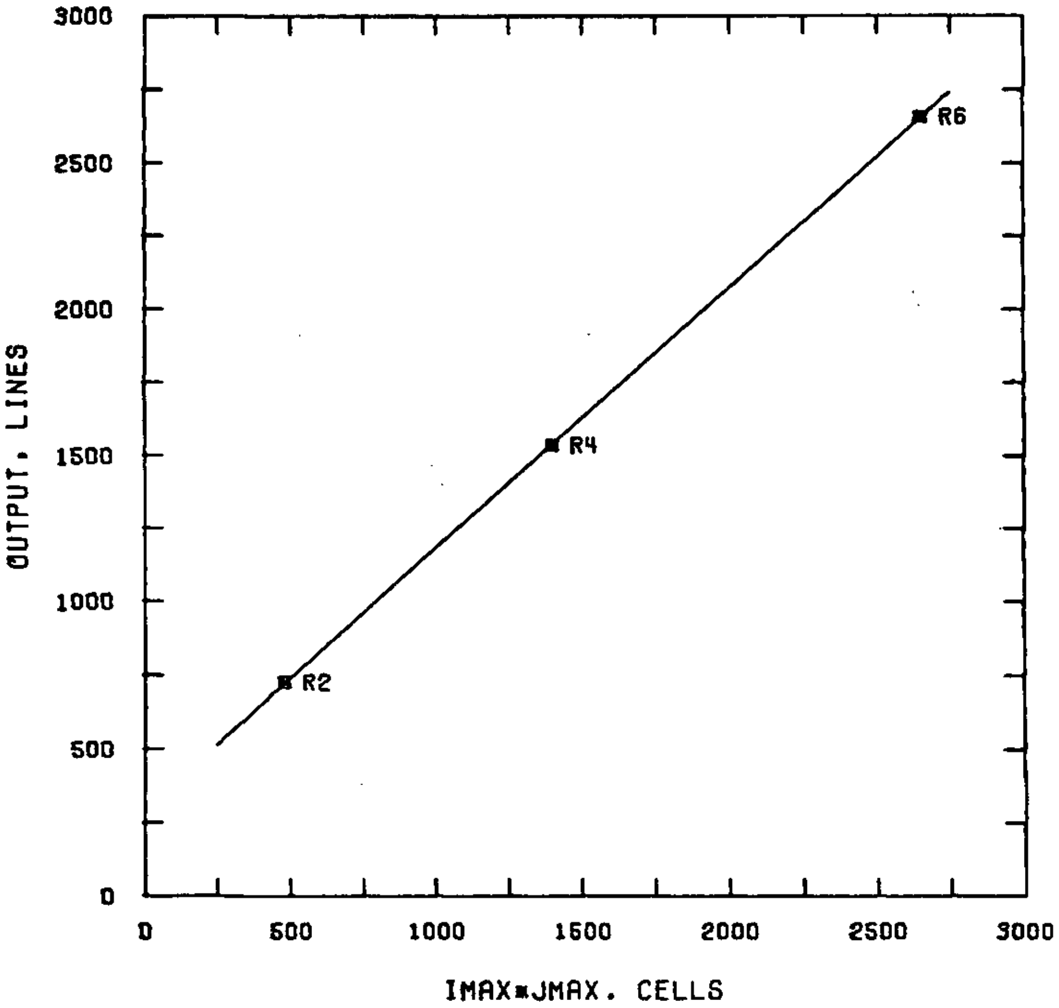

Figure 5. Relation Between the Number of Lines in the Computer Printout and the Total Number of Cells in the Grid

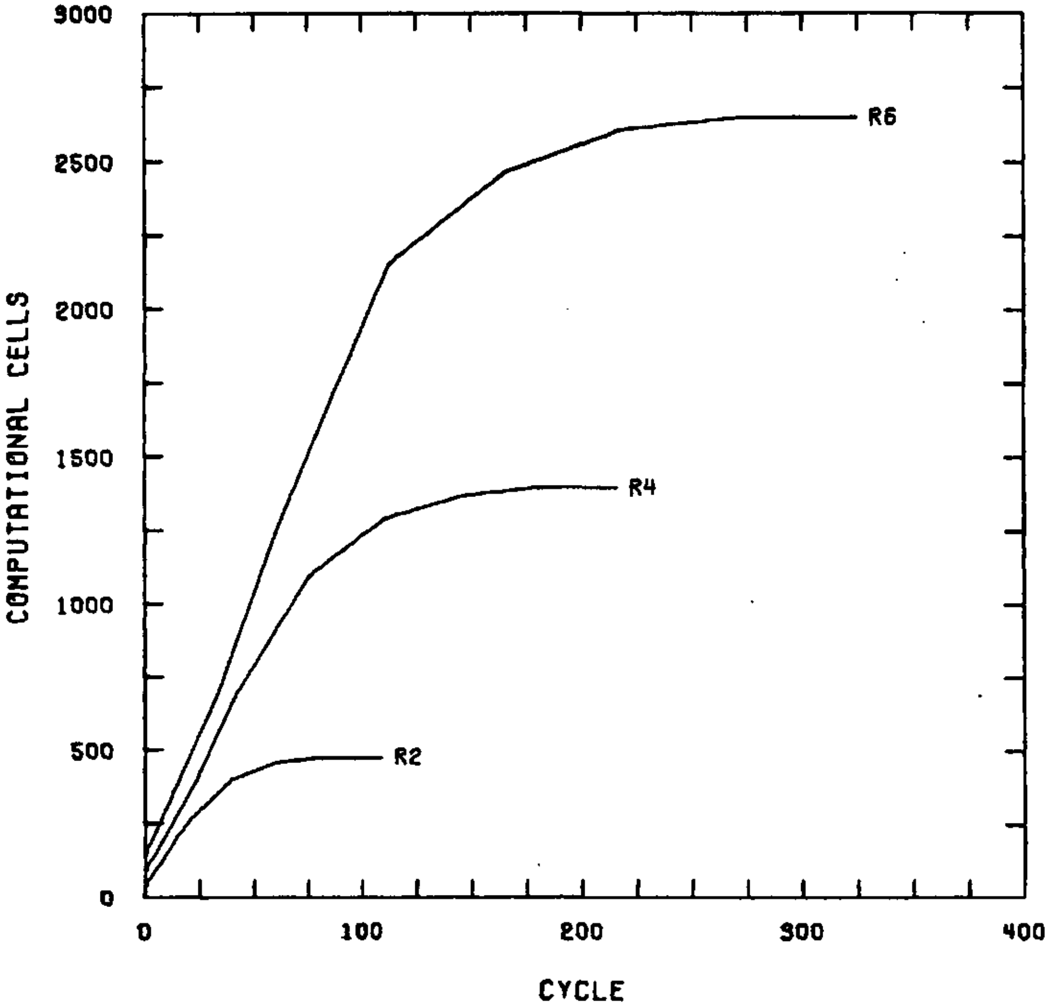

Figure 6. Growth of the Number of Active Computational Cells as the Computations Progress

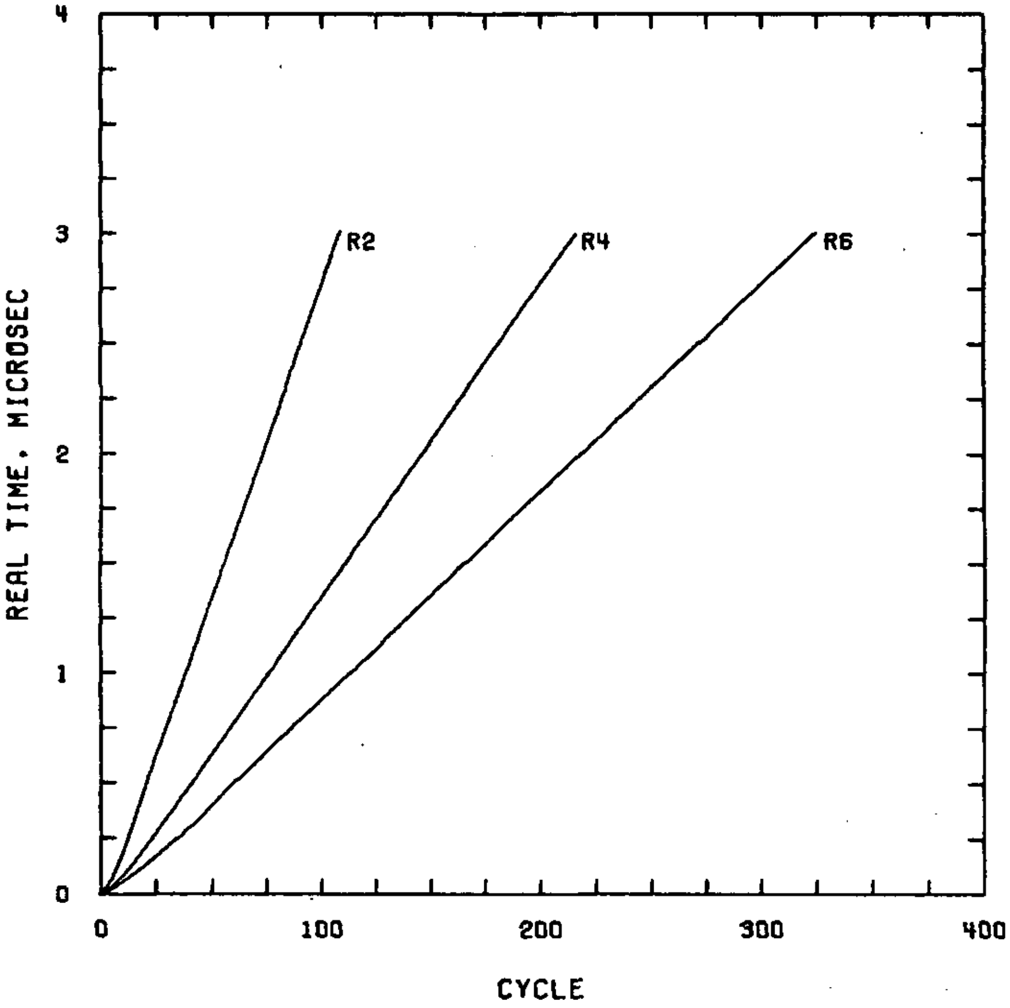

Figure 7. Real Time vs Number of Computational Cycles

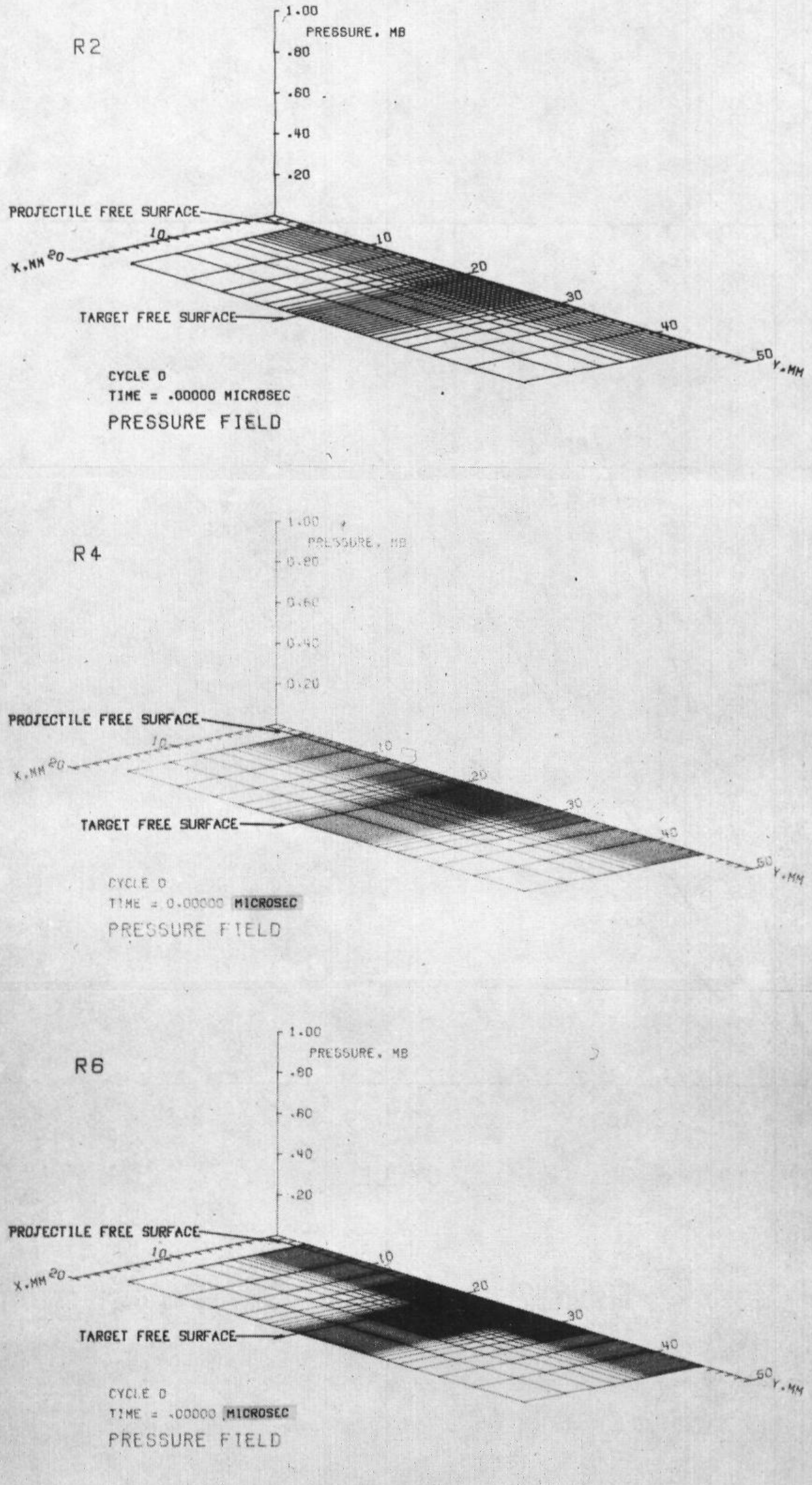

FIGURE 8. COMPARISON OF PRESSURE FIELDS

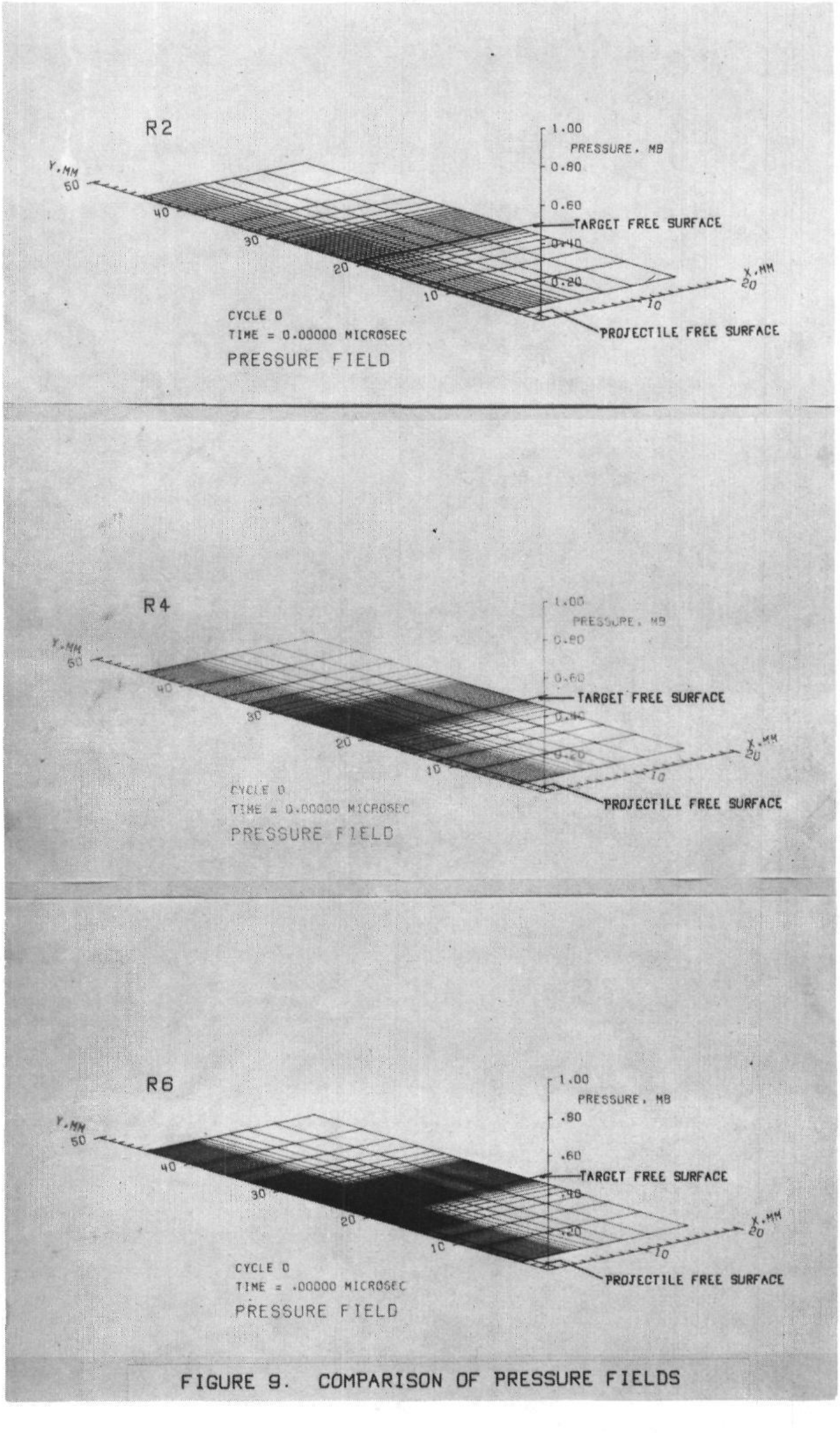

FIGURE 9. COMPARISON OF PRESSURE FIELDS

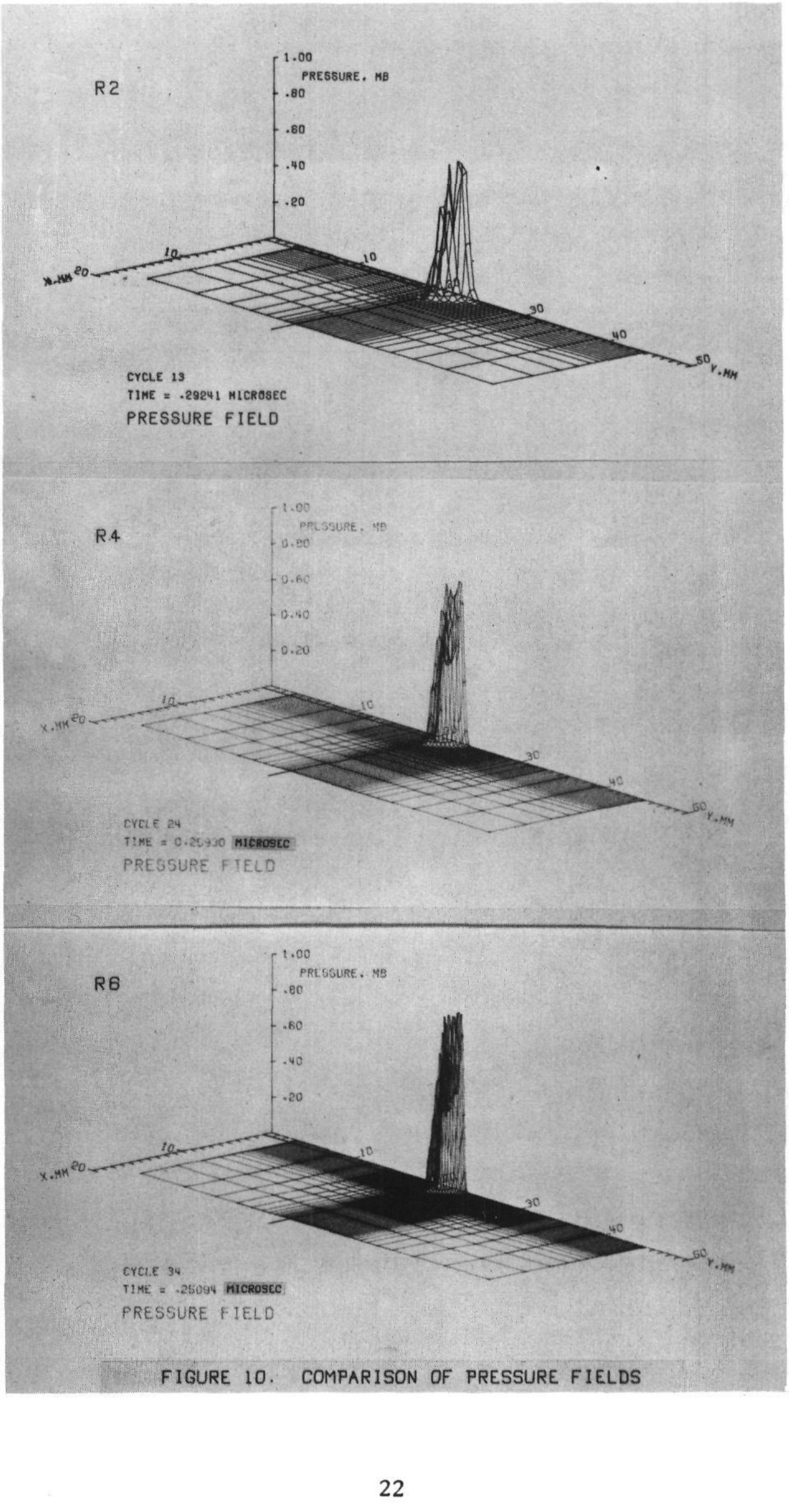

FIGURE 10. COMPARISON OF PRESSURE FIELDS

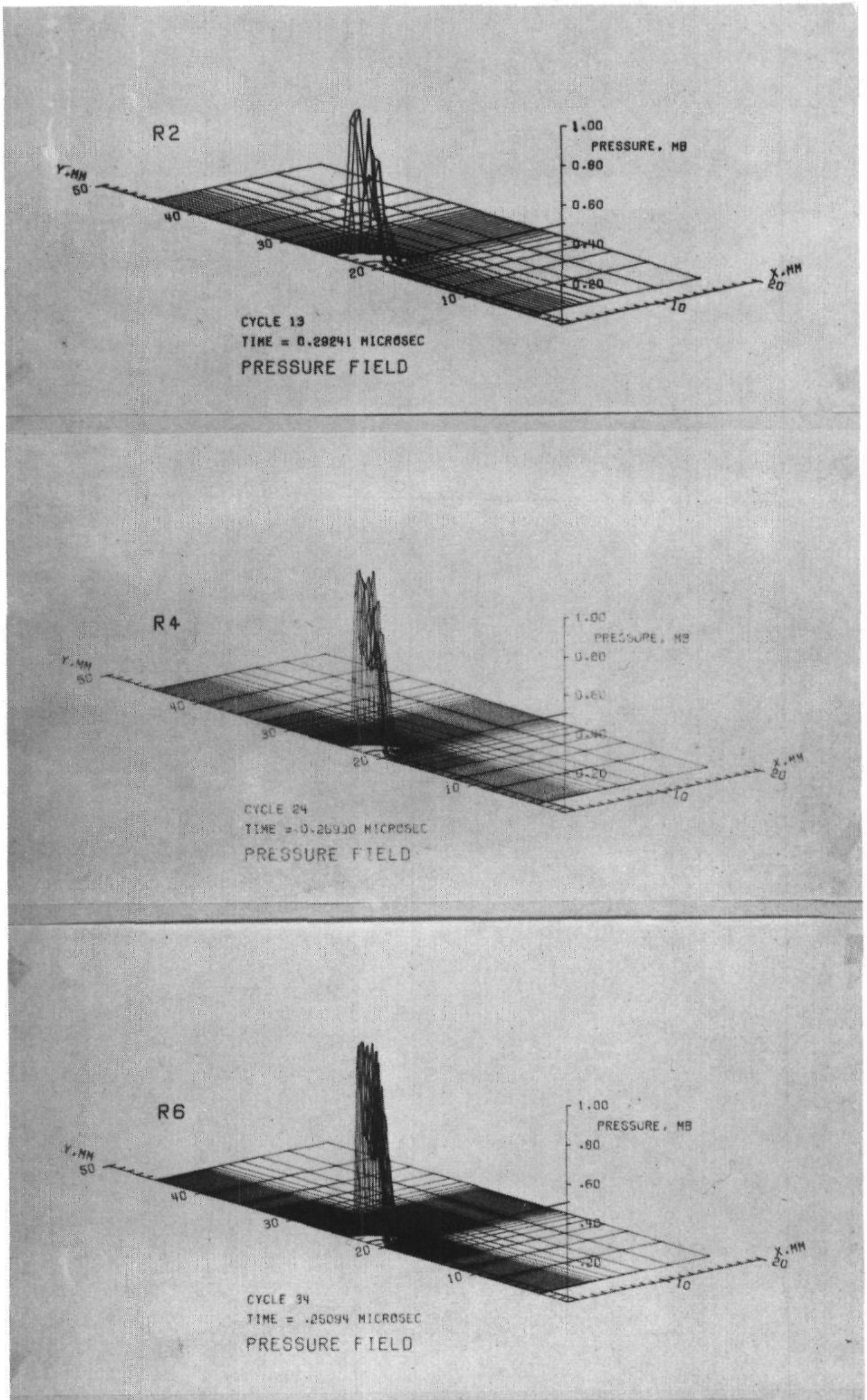

FIGURE 11. COMPARISON OF PRESSURE FIELDS

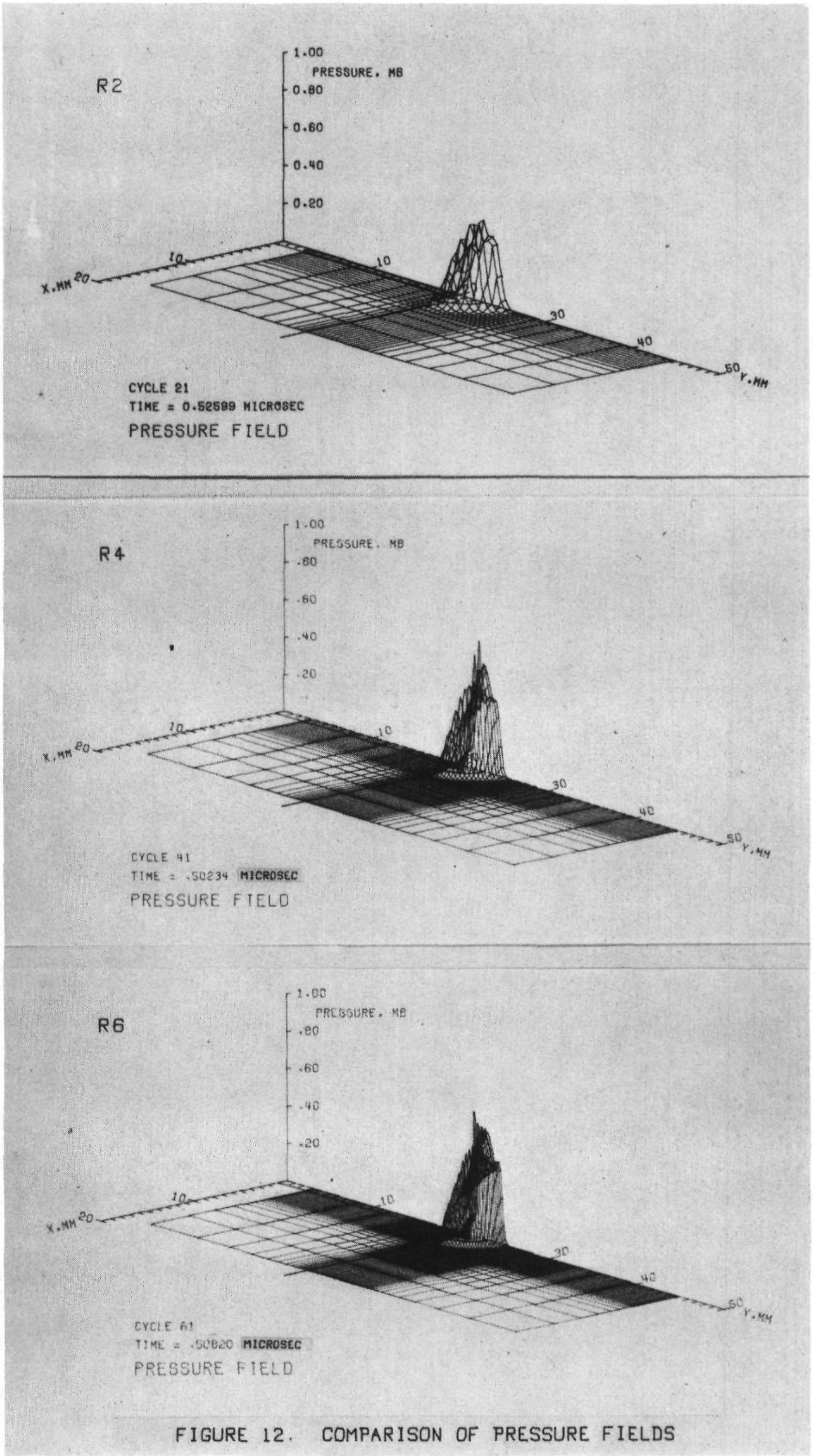

FIGURE 12. COMPARISON OF PRESSURE FIELDS

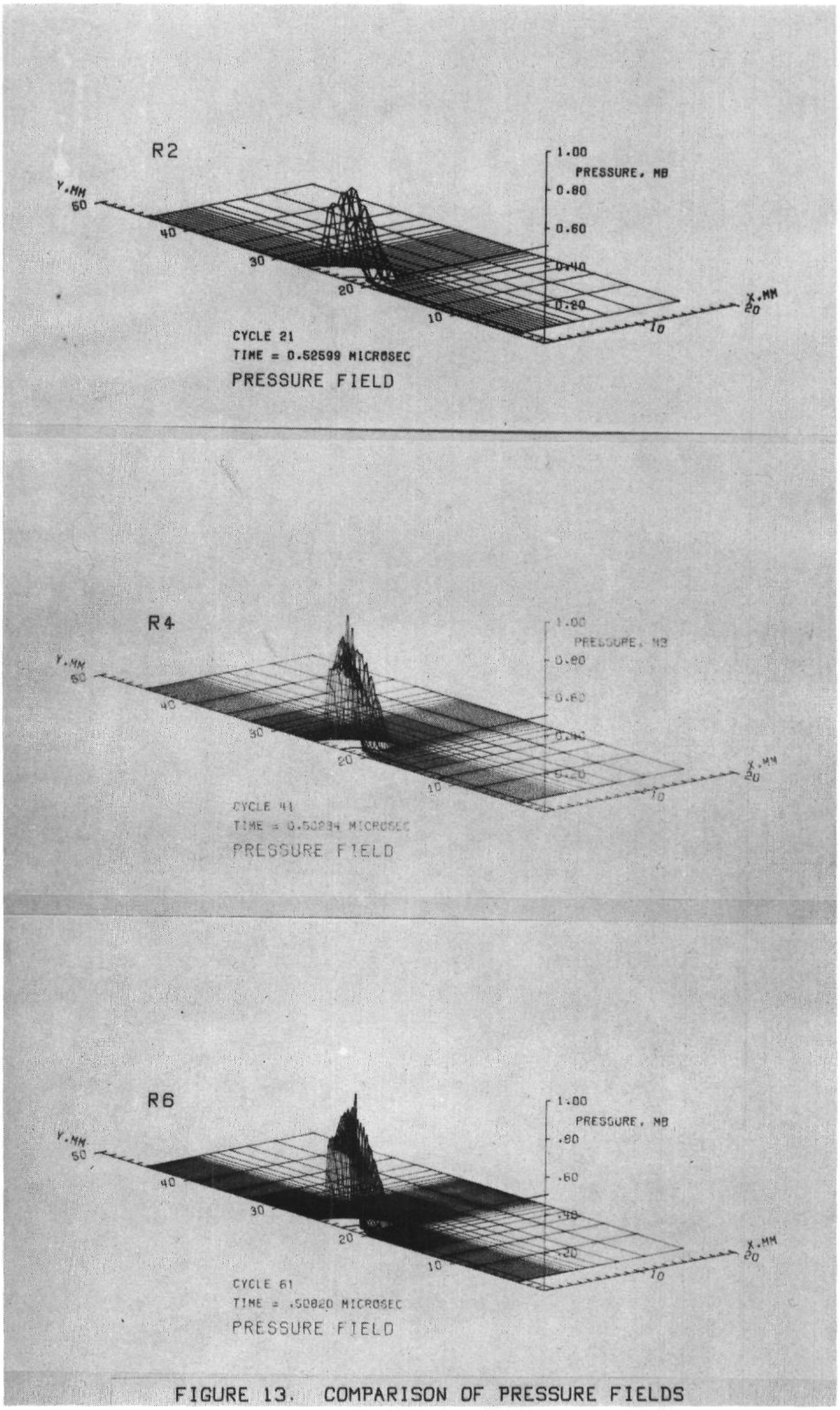

FIGURE 13. COMPARISON OF PRESSURE FIELDS

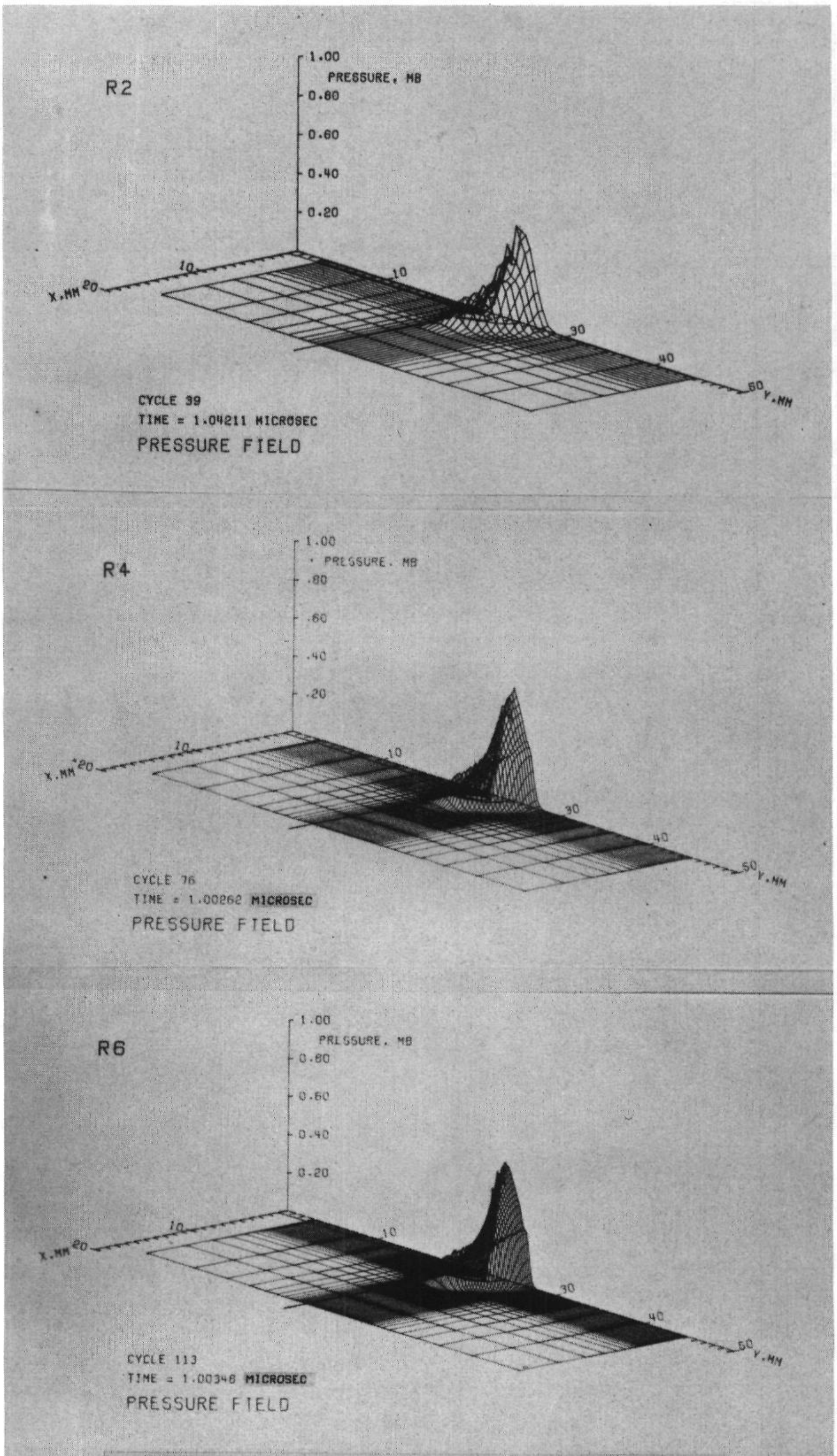

FIGURE 14. COMPARISON OF PRESSURE FIELDS

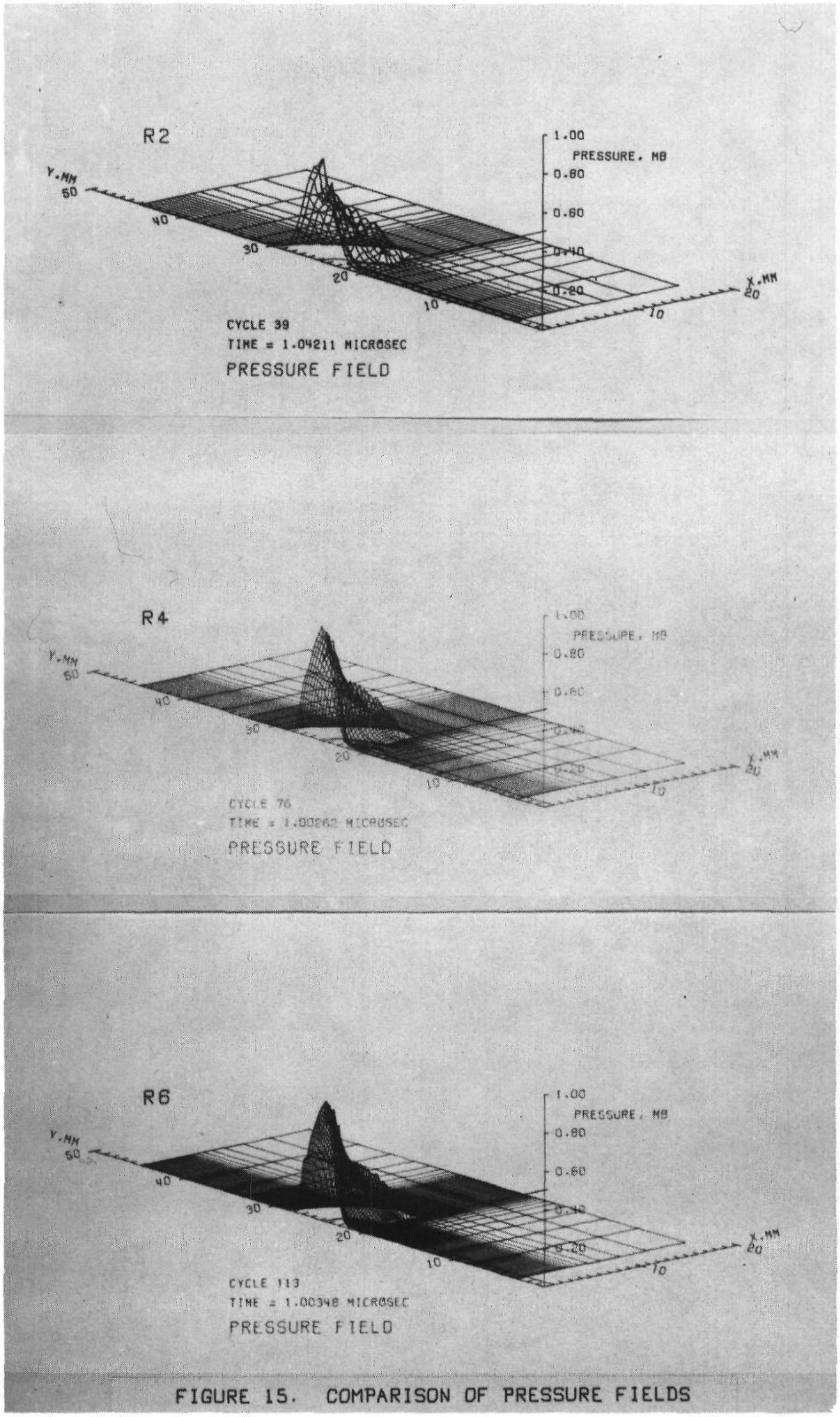

FIGURE 15. COMPARISON OF PRESSURE FIELDS

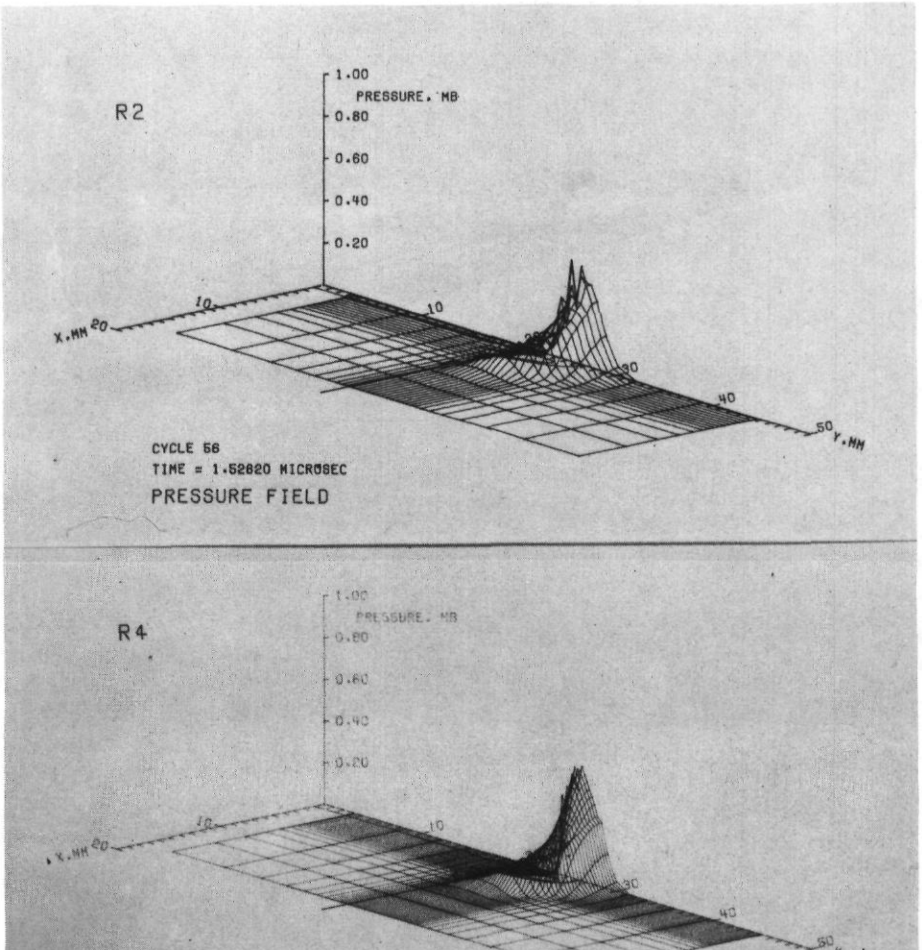

FIGURE 16. COMPARISON OF PRESSURE FIELDS

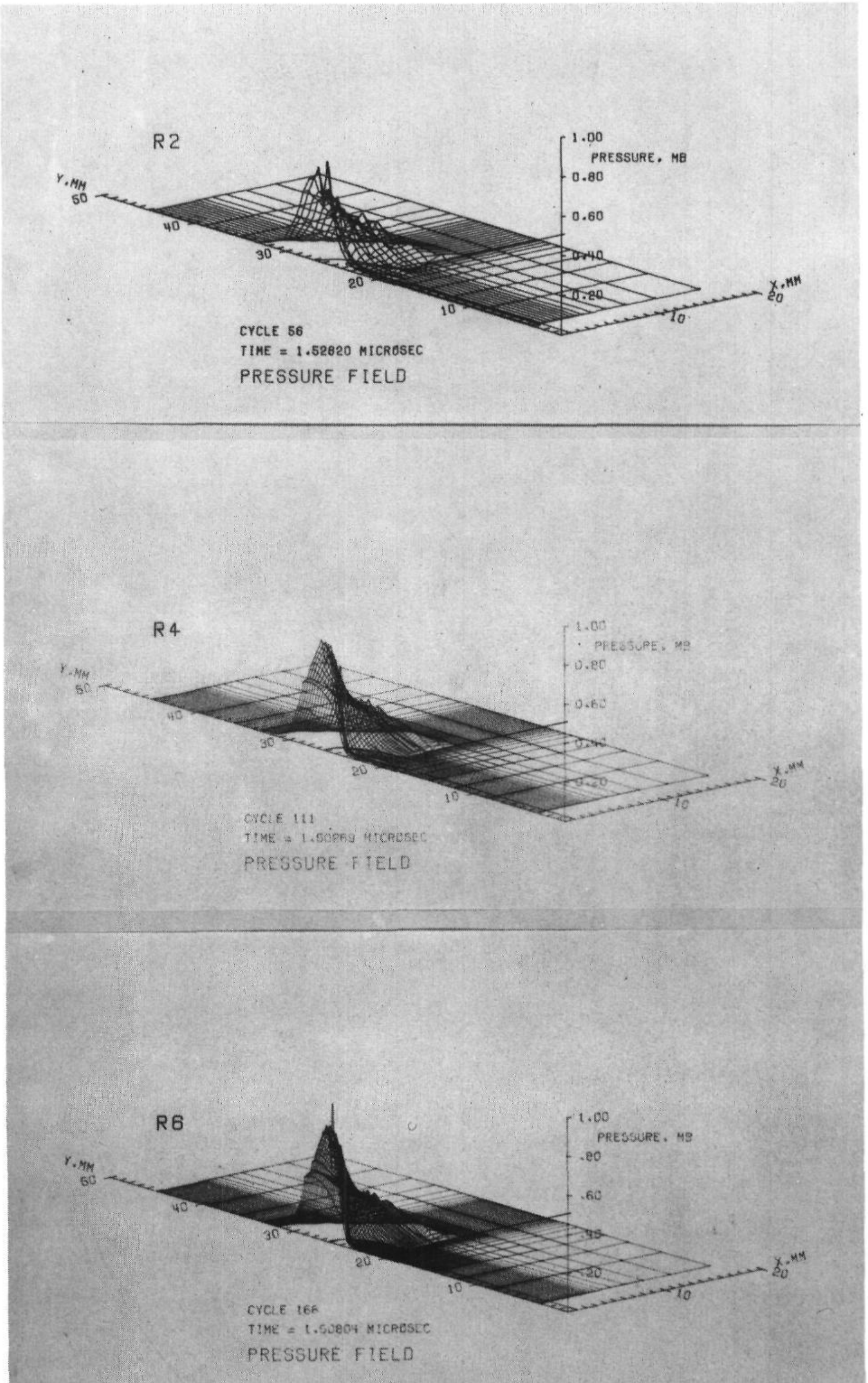

FIGURE 17. COMPARISON OF PRESSURE FIELDS

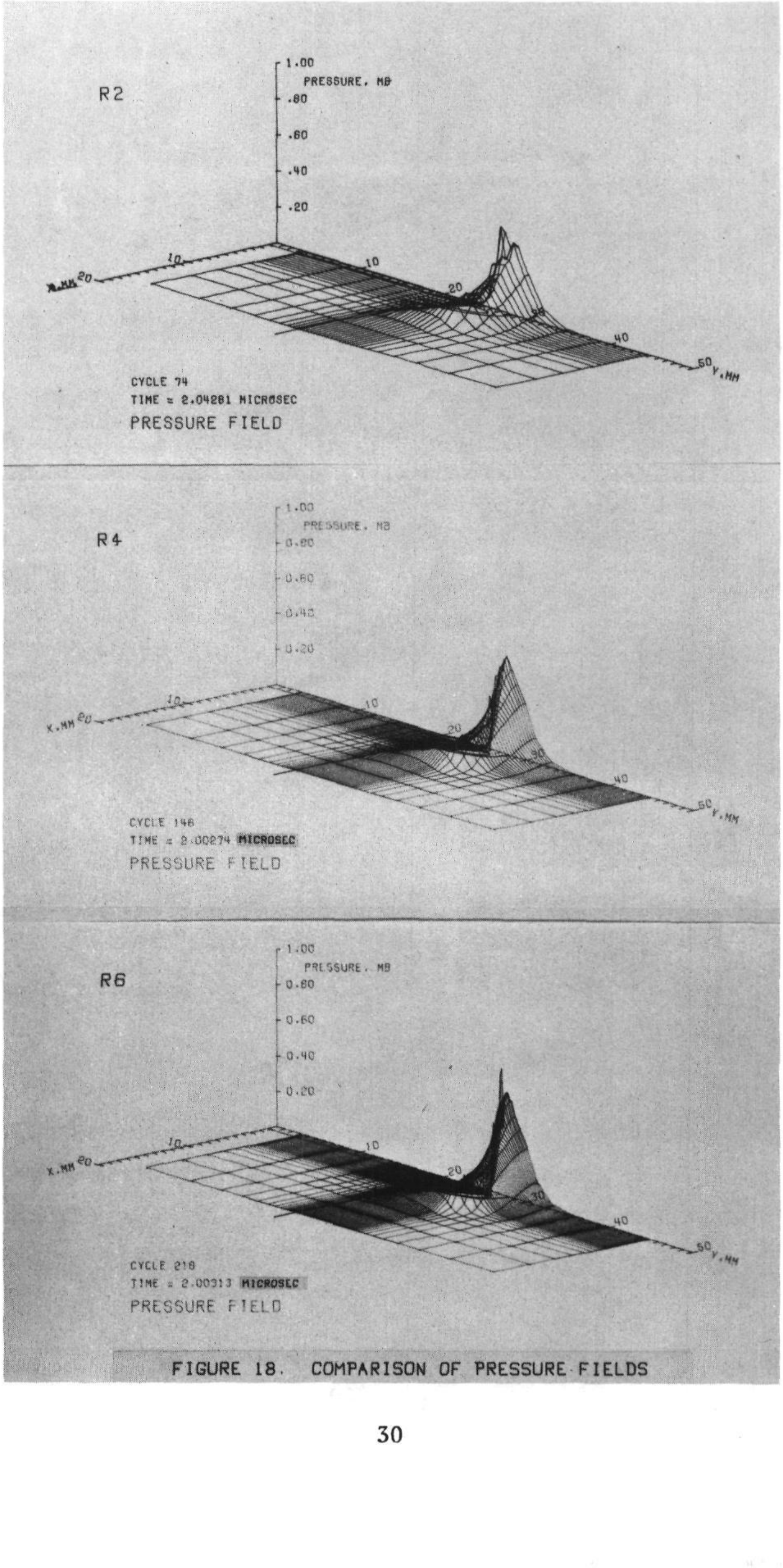

FIGURE 18. COMPARISON OF PRESSURE FIELDS

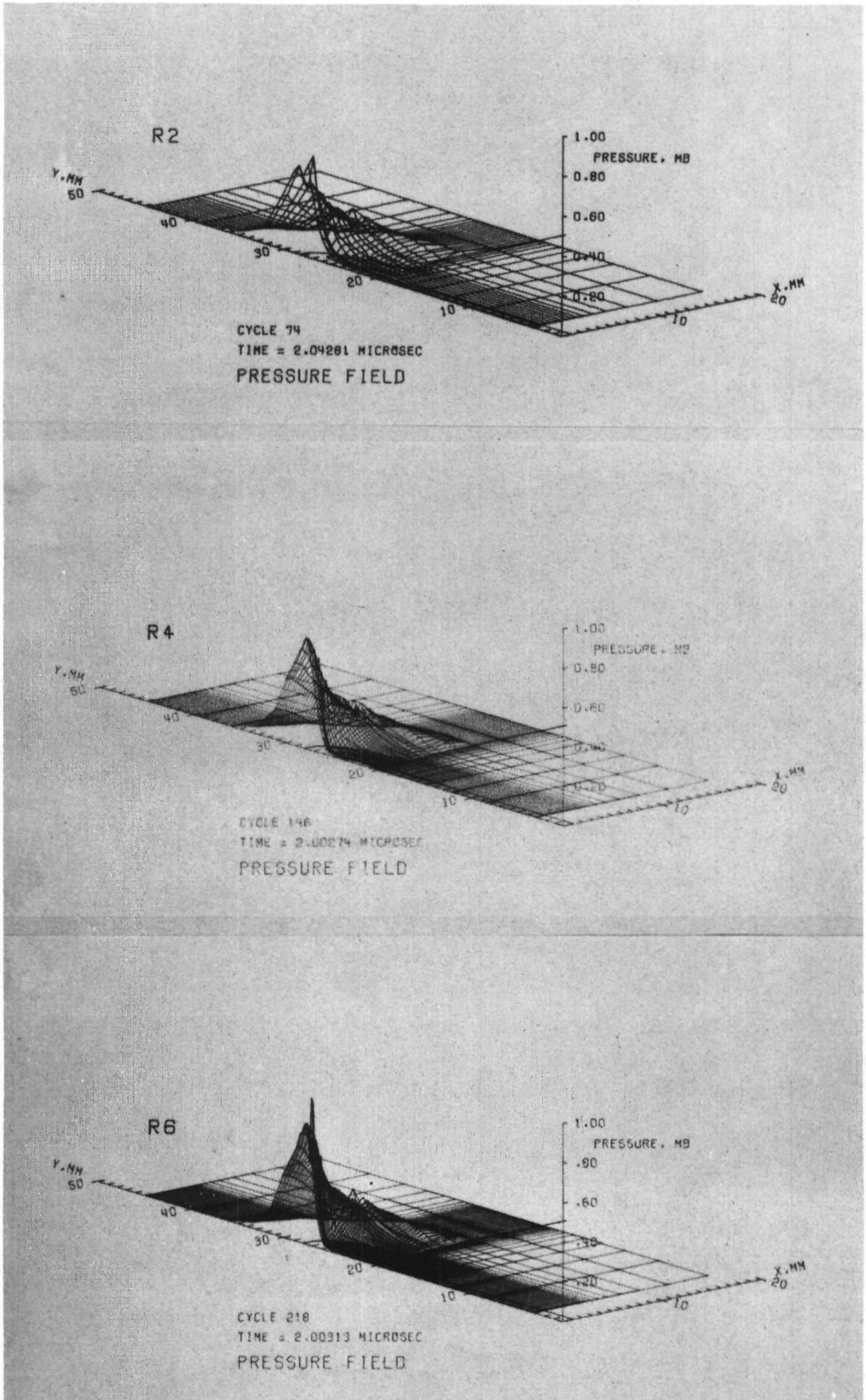

FIGURE 19. COMPARISON OF PRESSURE FIELDS

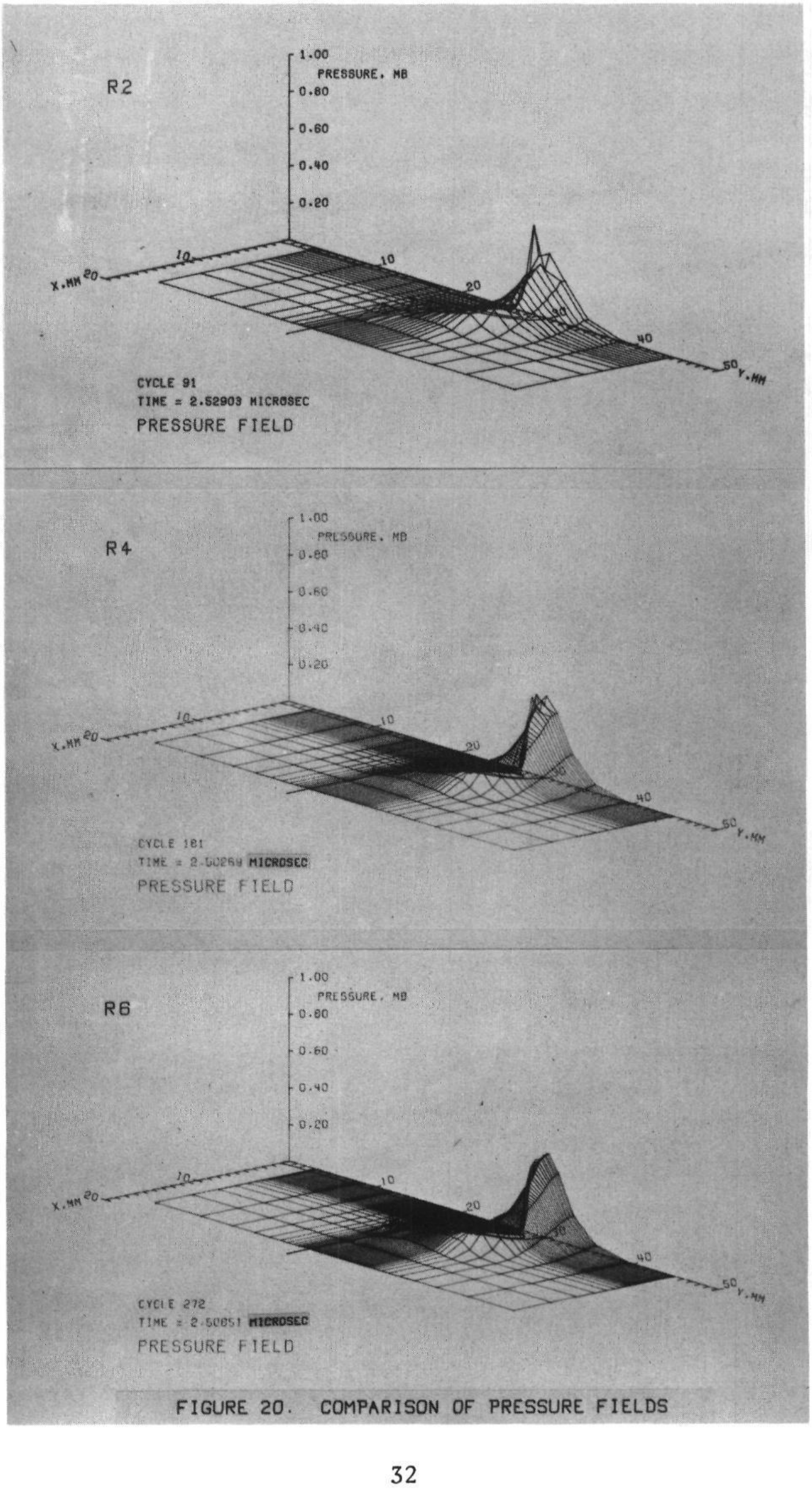

FIGURE 20. COMPARISON OF PRESSURE FIELDS

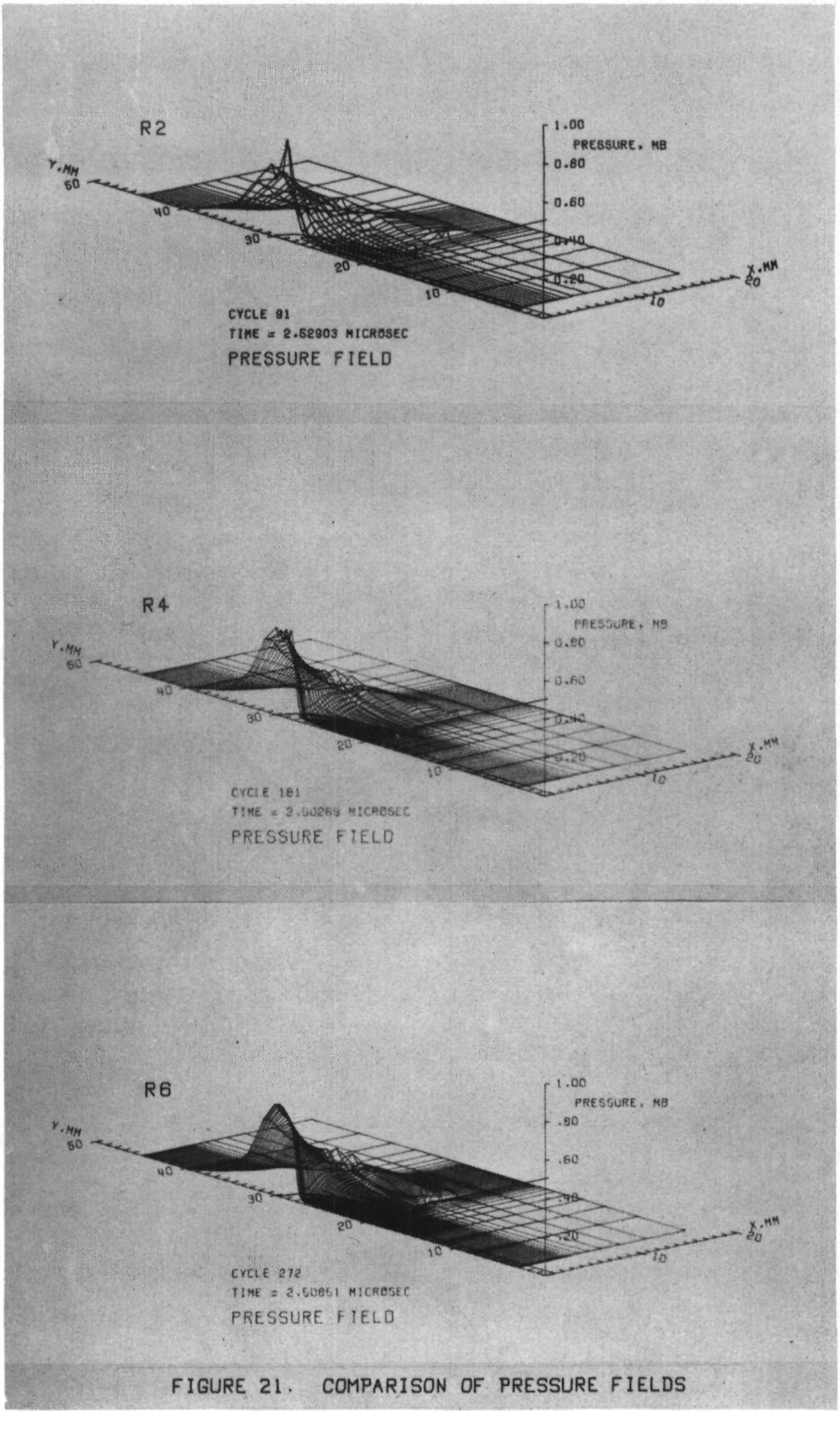

FIGURE 21. COMPARISON OF PRESSURE FIELDS

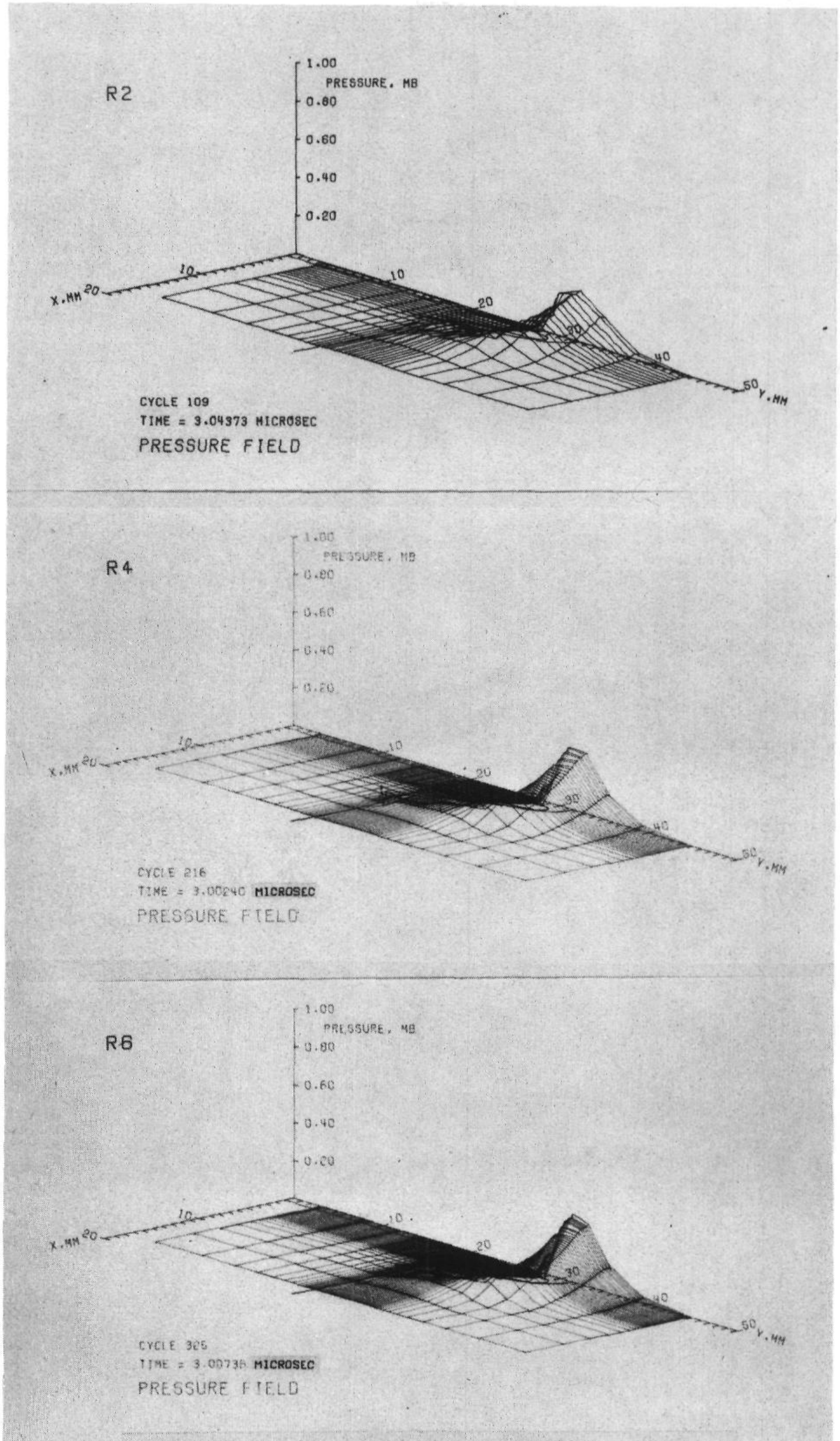

FIGURE 22. COMPARISON OF PRESSURE FIELDS

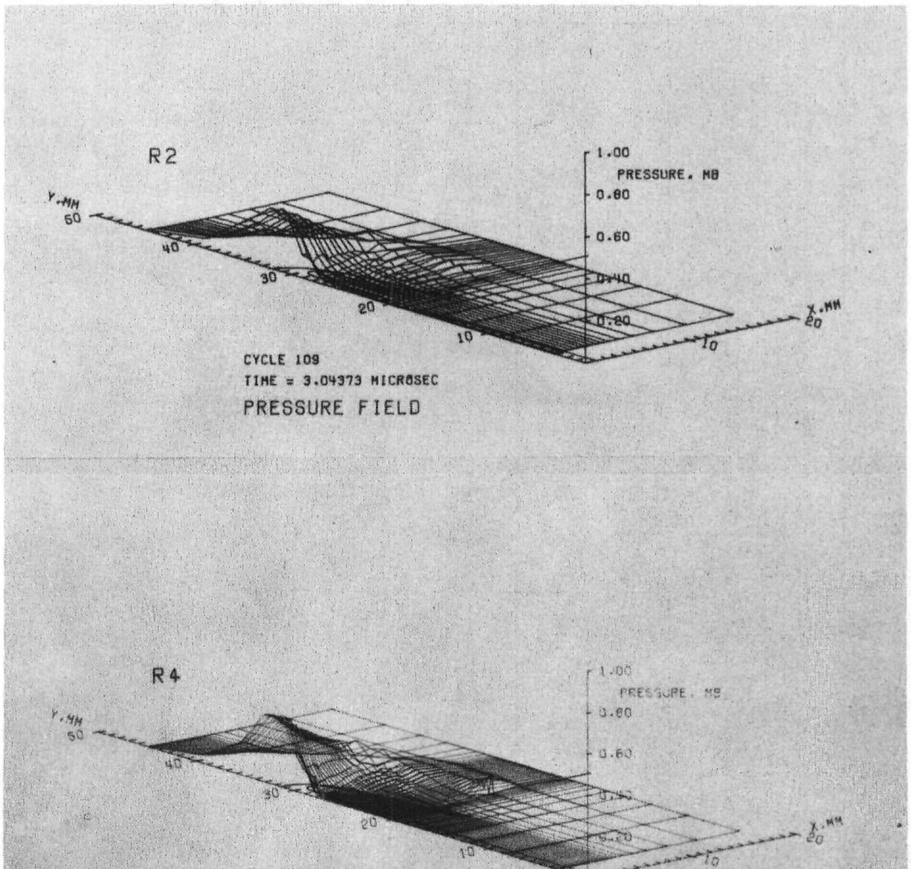

FIGURE 23. COMPARISON OF PRESSURE FIELDS

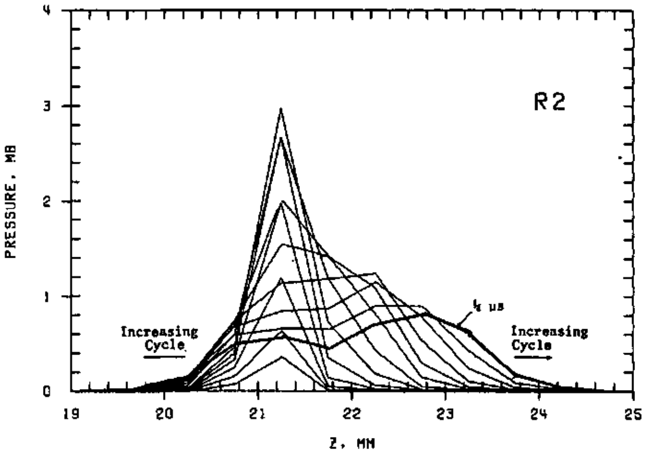

FIGURE 24. PRESSURE ALONG THE AXIS OF SYMMETRY

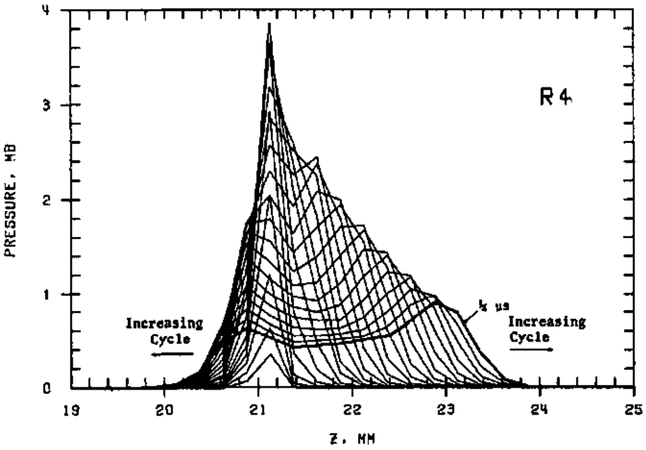

FIGURE 25. PRESSURE ALONG THE AXIS OF SYMMETRY

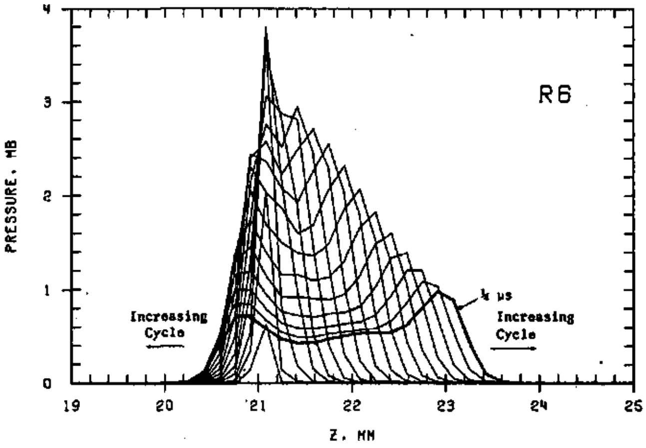

FIGURE 26. PRESSURE ALONG THE AXIS OF SYMMETRY

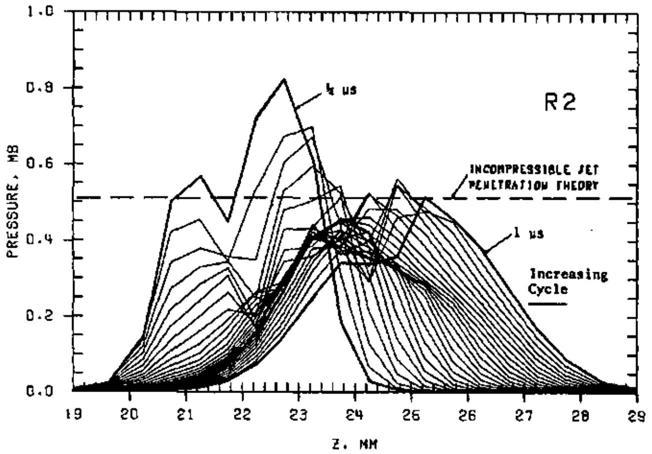

FIGURE 27. PRESSURE ALONG THE AXIS OF SYMMETRY

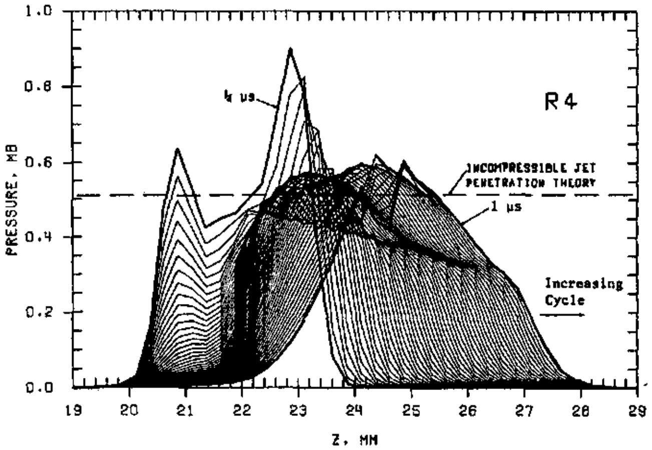

FIGURE 28. PRESSURE ALONG THE AXIS OF SYMMETRY

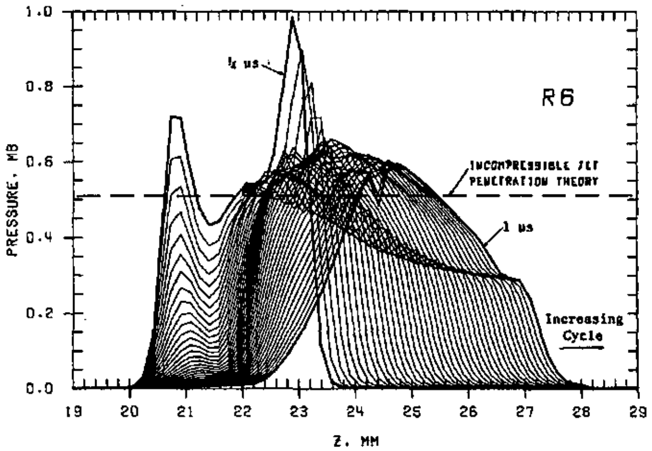

FIGURE 29. PRESSURE ALONG THE AXIS OF SYMMETRY

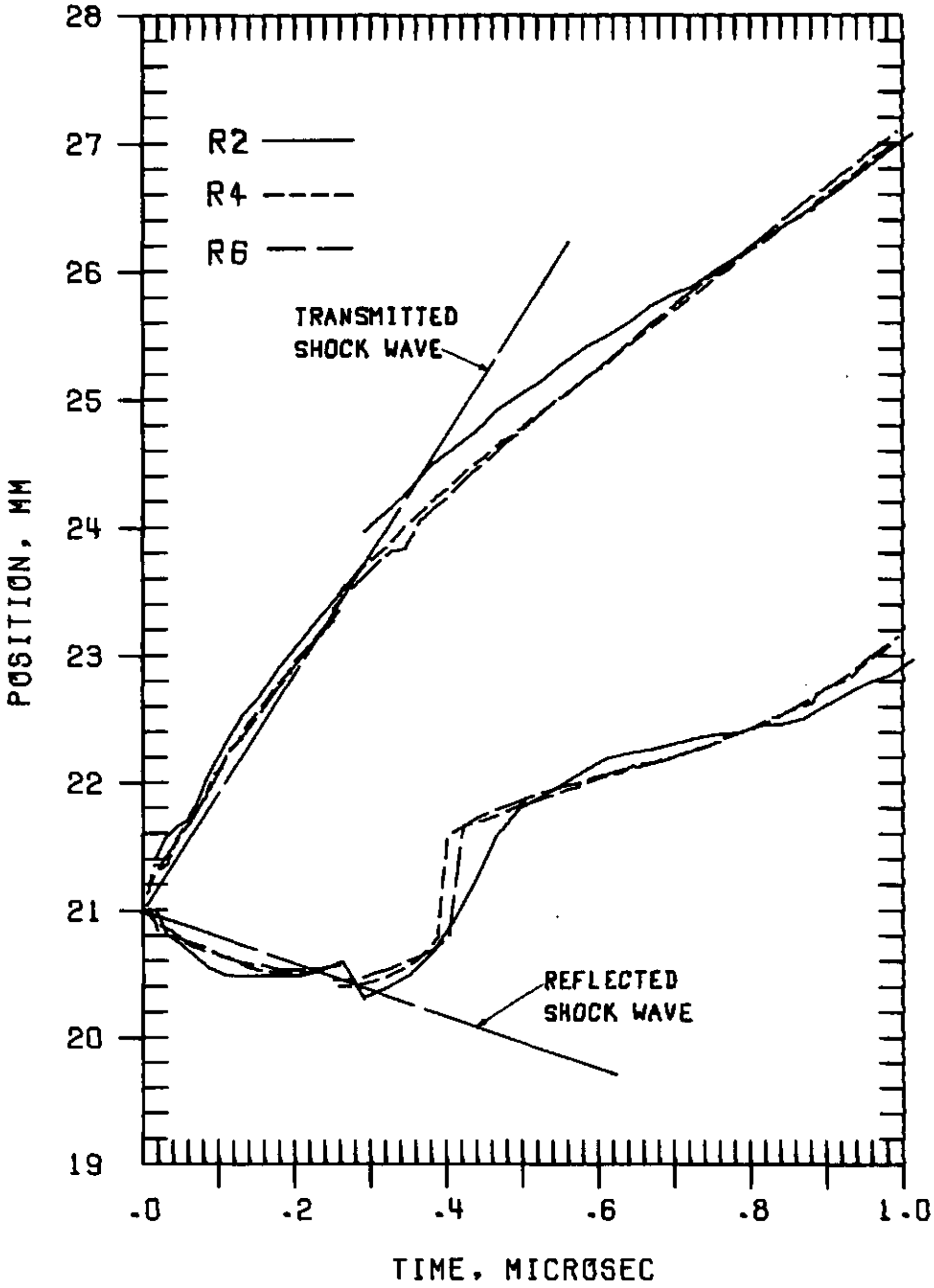

Figure 30. Wave Position vs Time

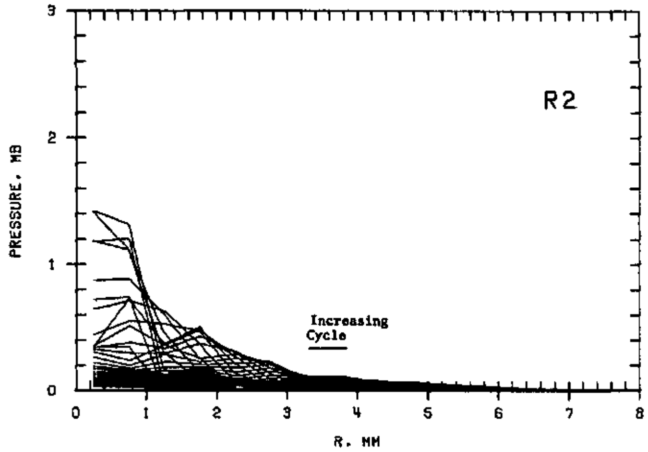

FIGURE 31. PRESSURE ALONG A CONSTANT Z COORDINATE

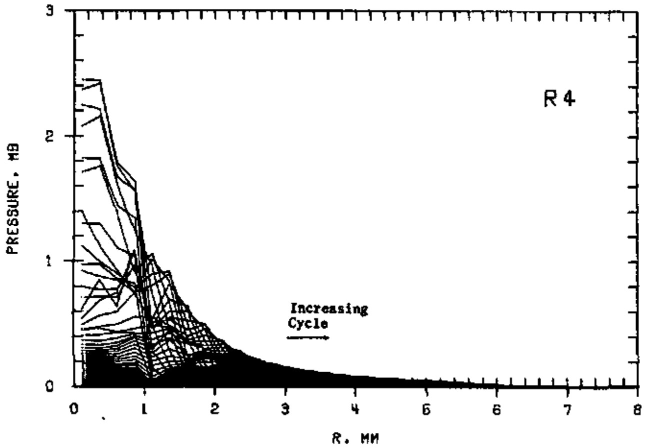

FIGURE 32. PRESSURE ALONG A CONSTANT Z COORDINATE

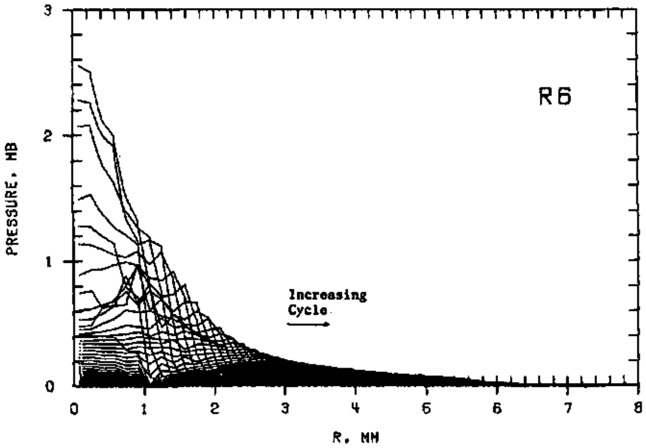

FIGURE 33. PRESSURE ALONG A CONSTANT Z COORDINATE

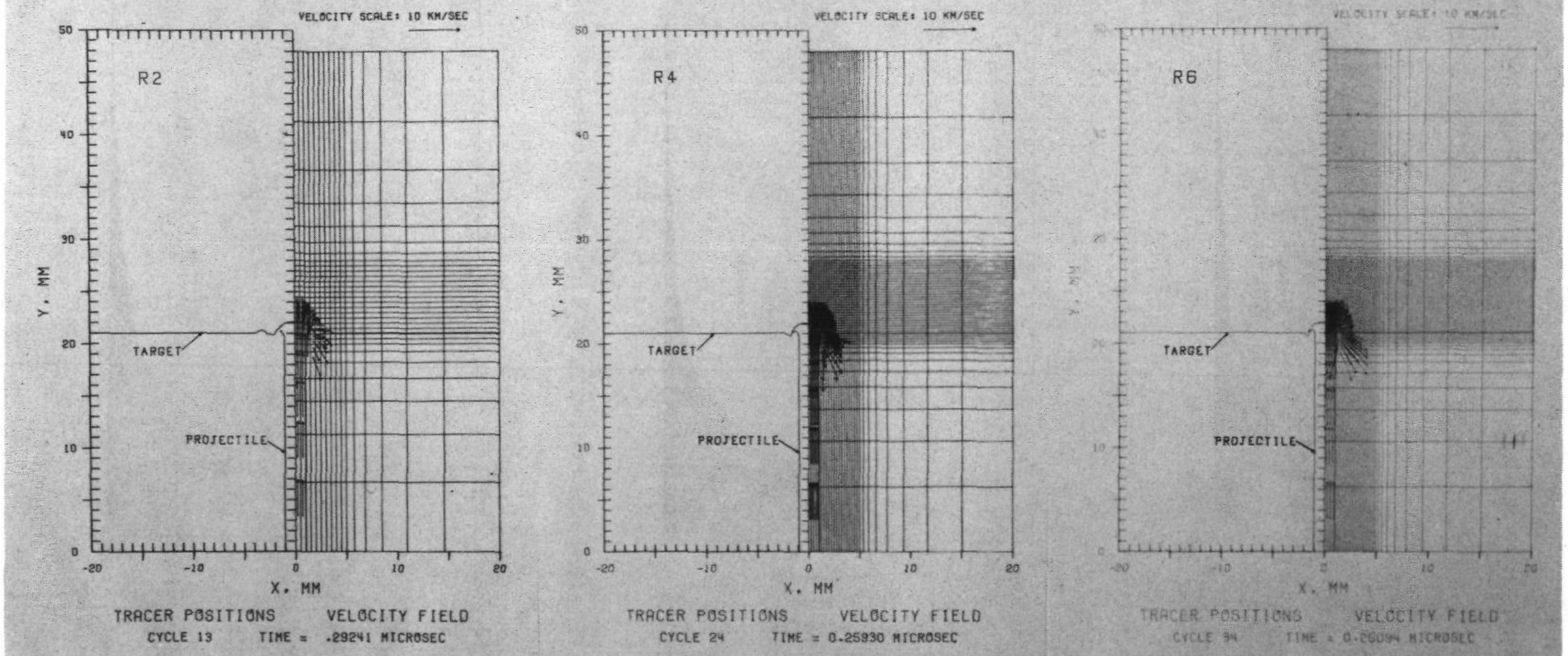

FIGURE 34. COMPARISON OF PROJECTILE-TARGET DEFORMATIONS AND VELOCITY FIELDS

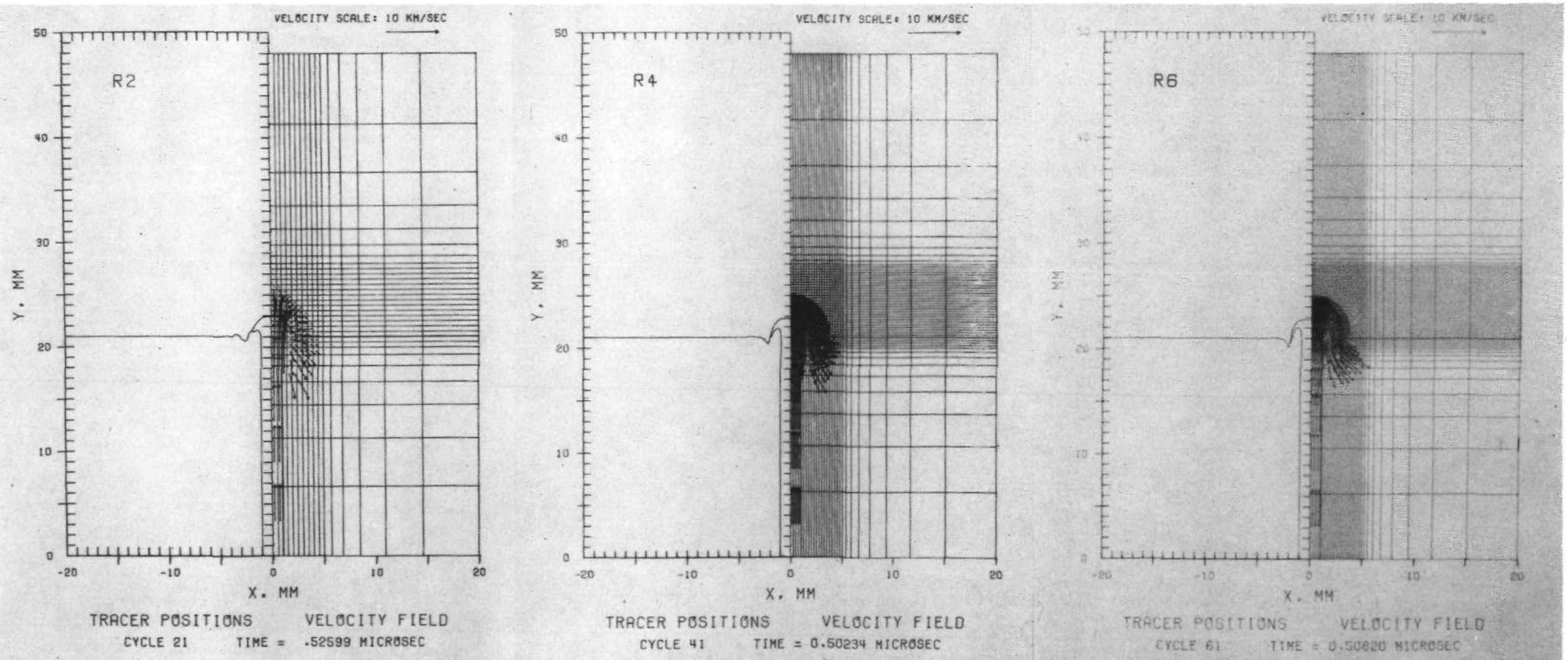

FIGURE 35. COMPARISON OF PROJECTILE-TARGET DEFORMATIONS AND VELOCITY FIELDS

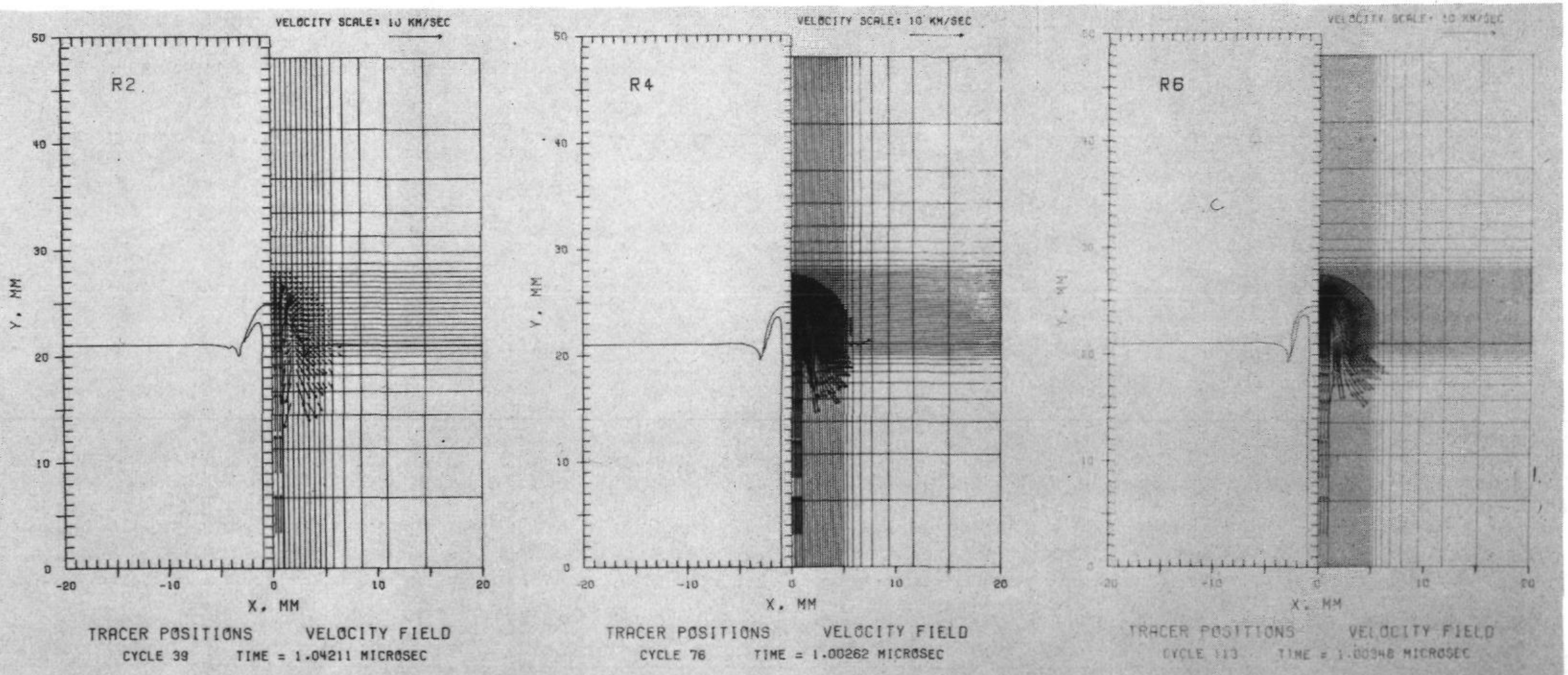

FIGURE 36. COMPARISON OF PROJECTILE-TARGET DEFORMATIONS AND VELOCITY FIELDS

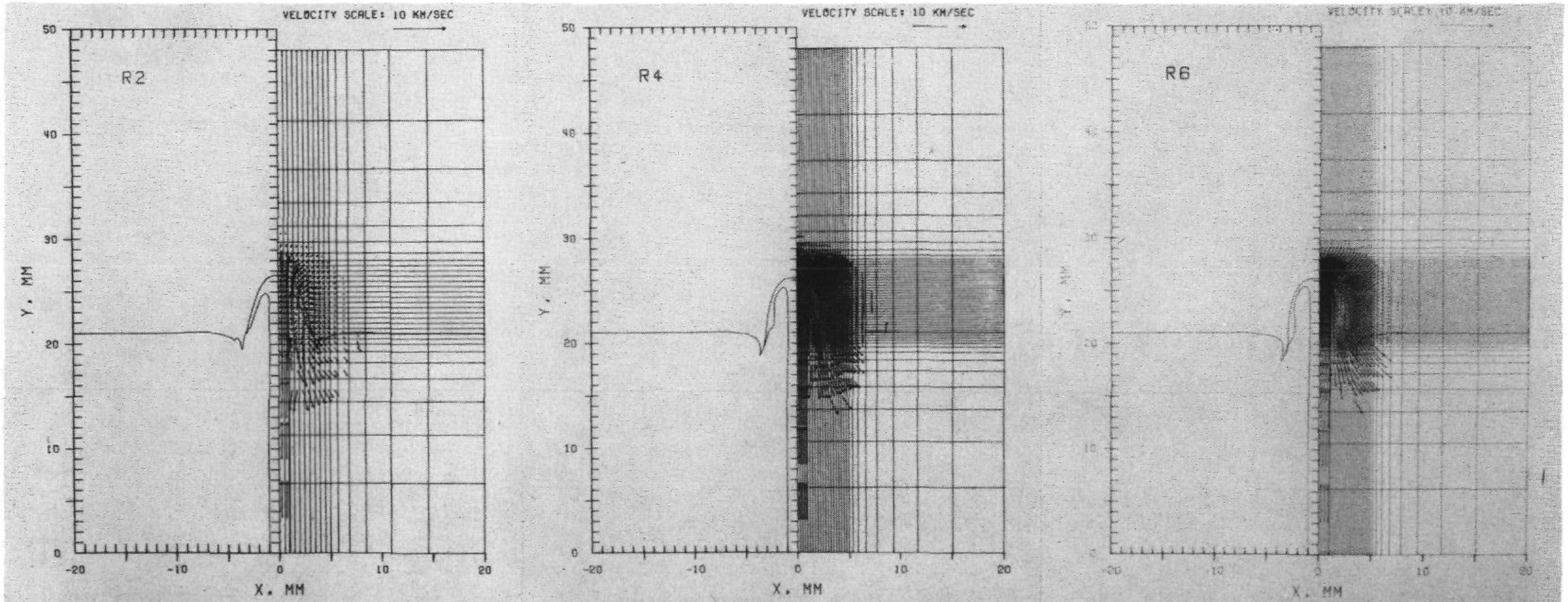

TRACER POSITIONS VELOCITY FIELD
CYCLE 56 TIME = 1.52820 MICROSEC

TRACER POSITIONS VELOCITY FIELD
CYCLE 111 TIME = 1.50269 MICROSEC

TRACER POSITIONS VELOCITY FIELD
CYCLE 166 TIME = 1.50804 MICROSEC

FIGURE 37. COMPARISON OF PROJECTILE-TARGET DEFORMATIONS AND VELOCITY FIELDS

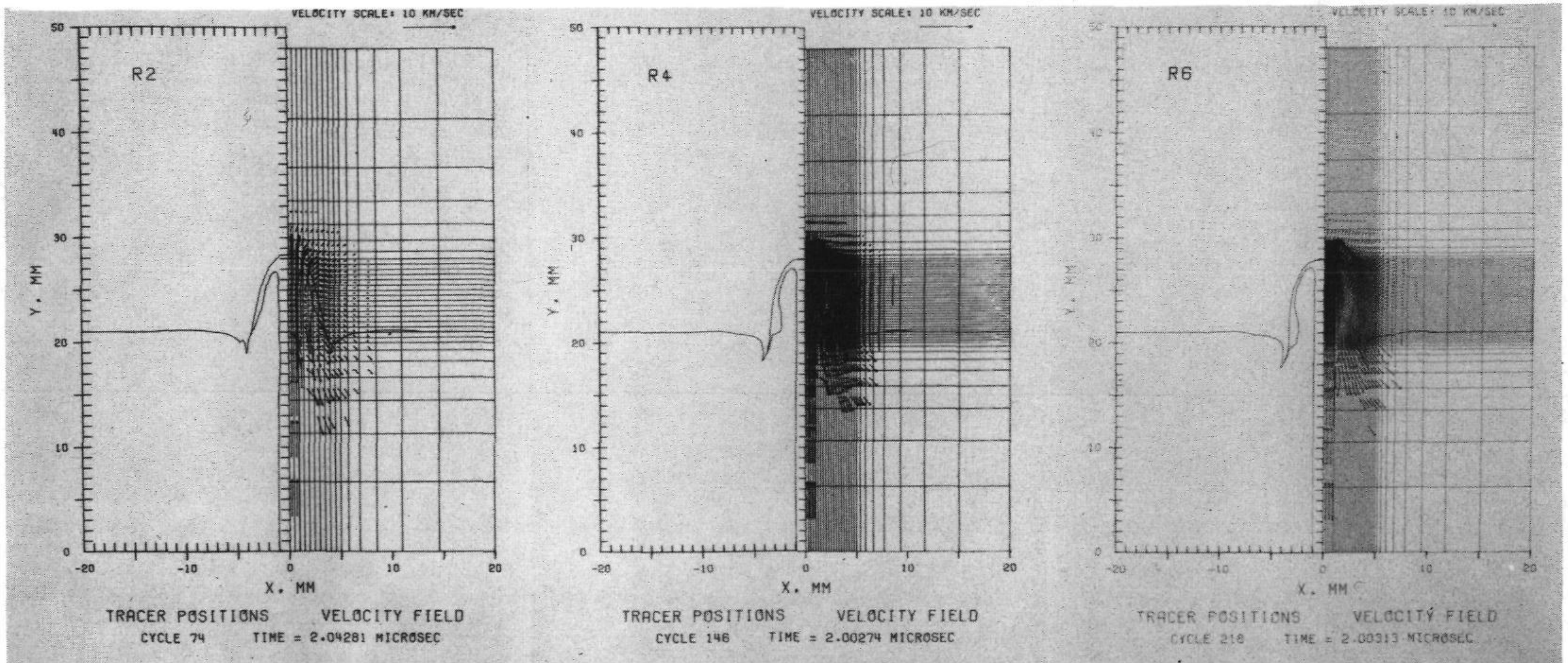

FIGURE 38. COMPARISON OF PROJECTILE-TARGET DEFORMATIONS AND VELOCITY FIELDS

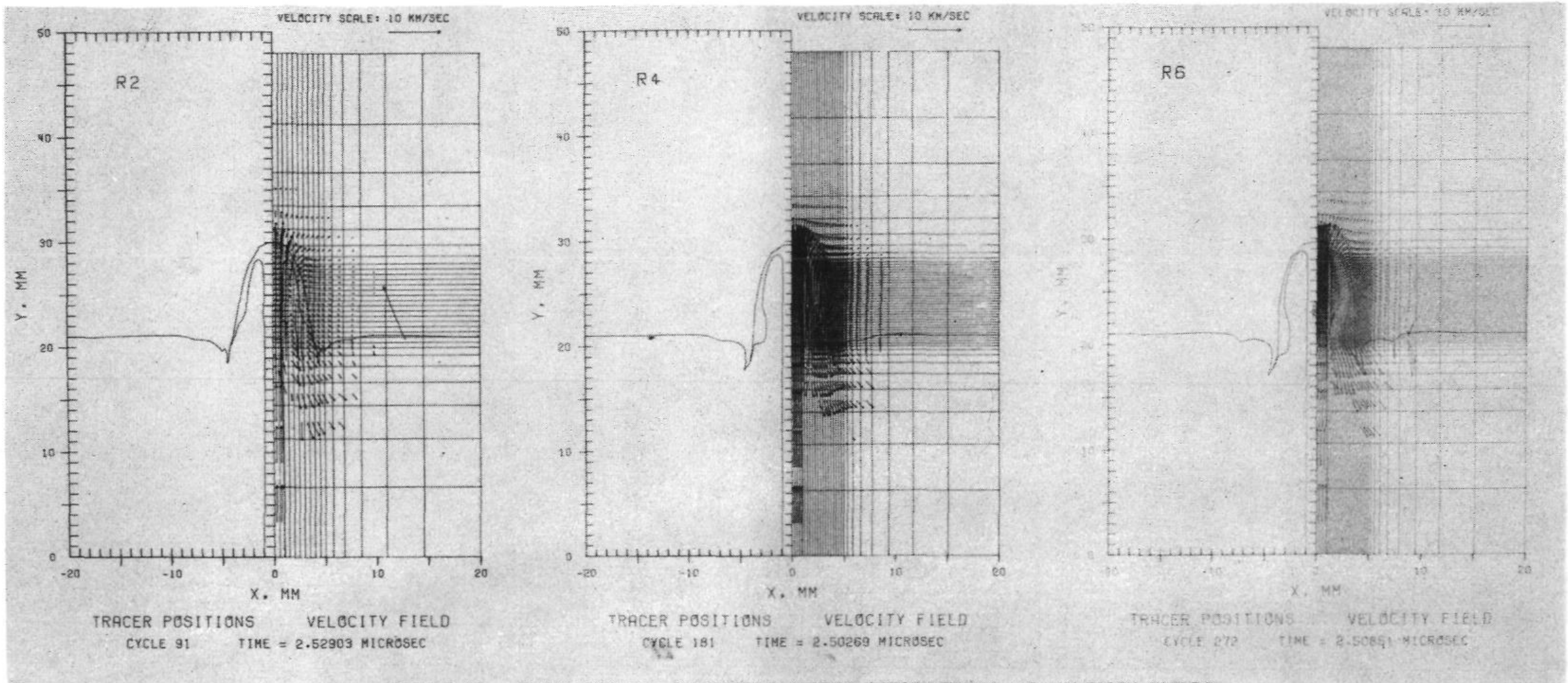

FIGURE 39. COMPARISON OF PROJECTILE-TARGET DEFORMATIONS AND VELOCITY FIELDS

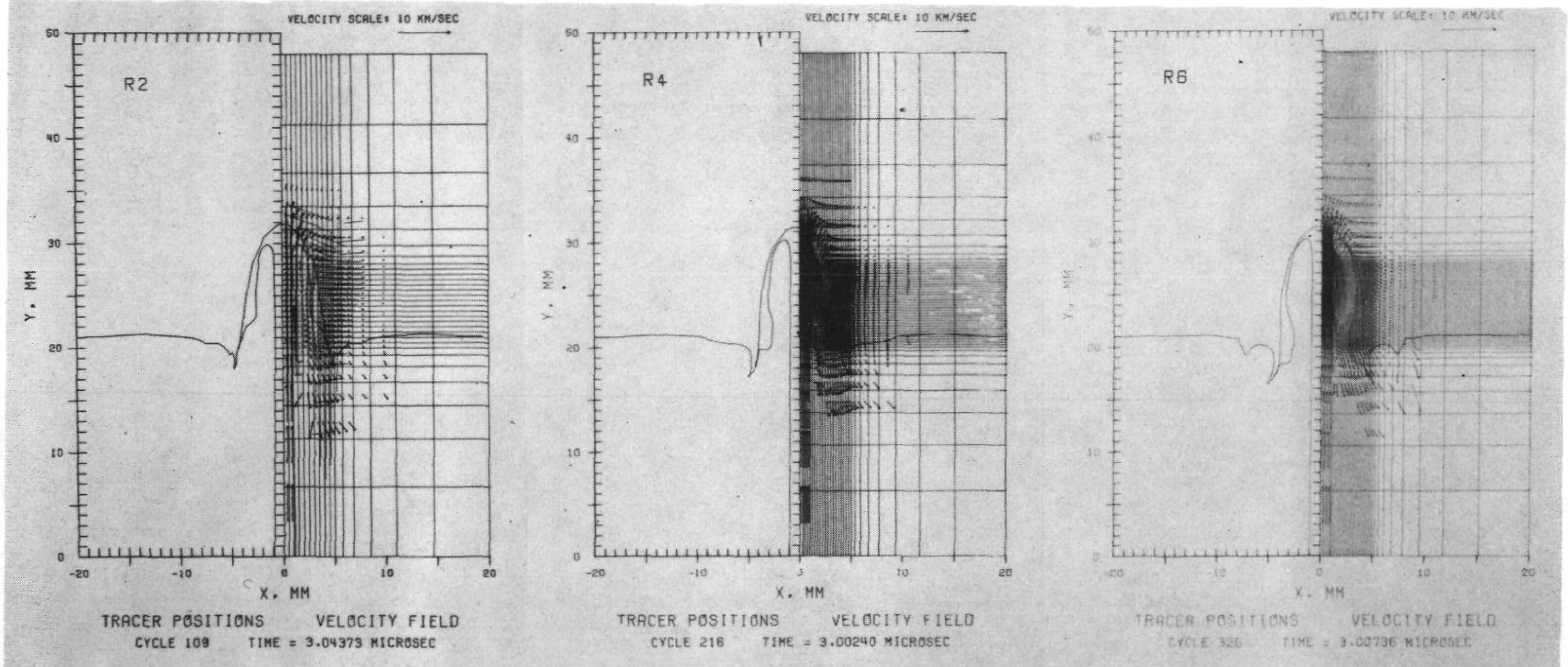

FIGURE 40. COMPARISON OF PROJECTILE-TARGET DEFORMATIONS AND VELOCITY FIELDS

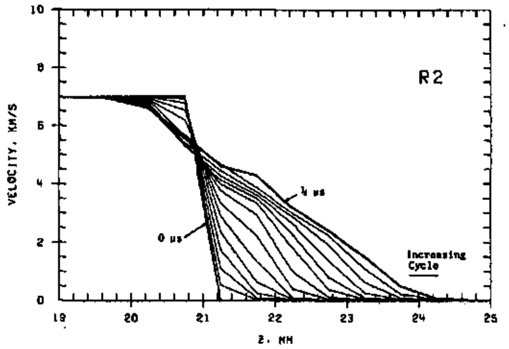

FIGURE 41. PARTICLE VELOCITY ALONG THE AXIS OF SYMMETRY

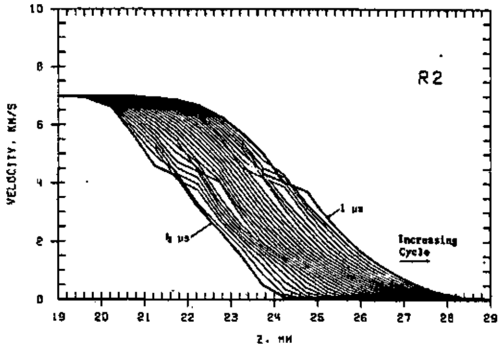

FIGURE 44. PARTICLE VELOCITY ALONG THE AXIS OF SYMMETRY

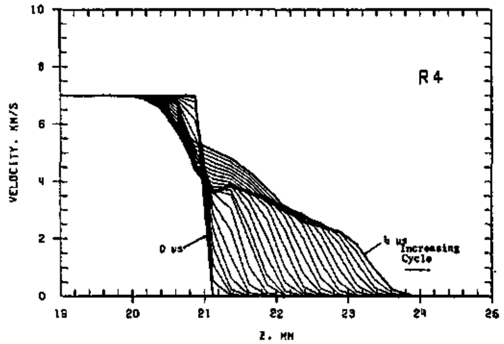

FIGURE 42. PARTICLE VELOCITY ALONG THE AXIS OF SYMMETRY

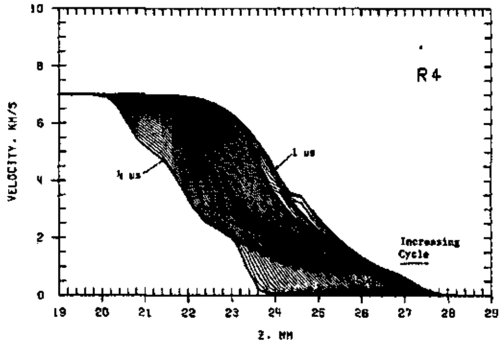

FIGURE 45. PARTICLE VELOCITY ALONG THE AXIS OF SYMMETRY

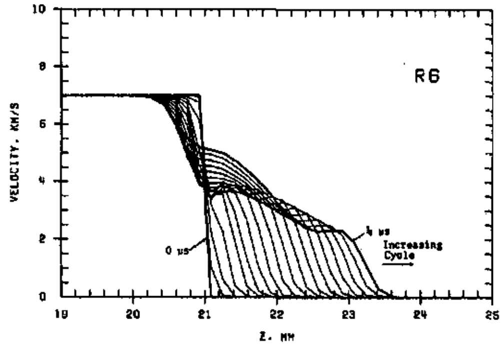

FIGURE 43. PARTICLE VELOCITY ALONG THE AXIS OF SYMMETRY

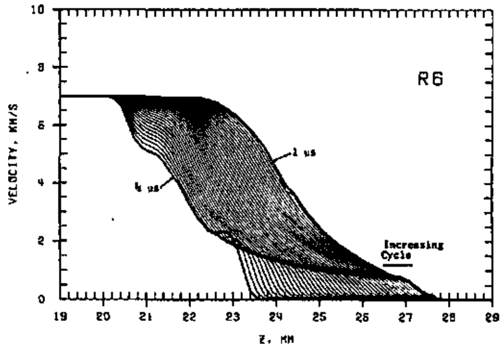

FIGURE 48. PARTICLE VELOCITY ALONG THE AXIS OF SYMMETRY

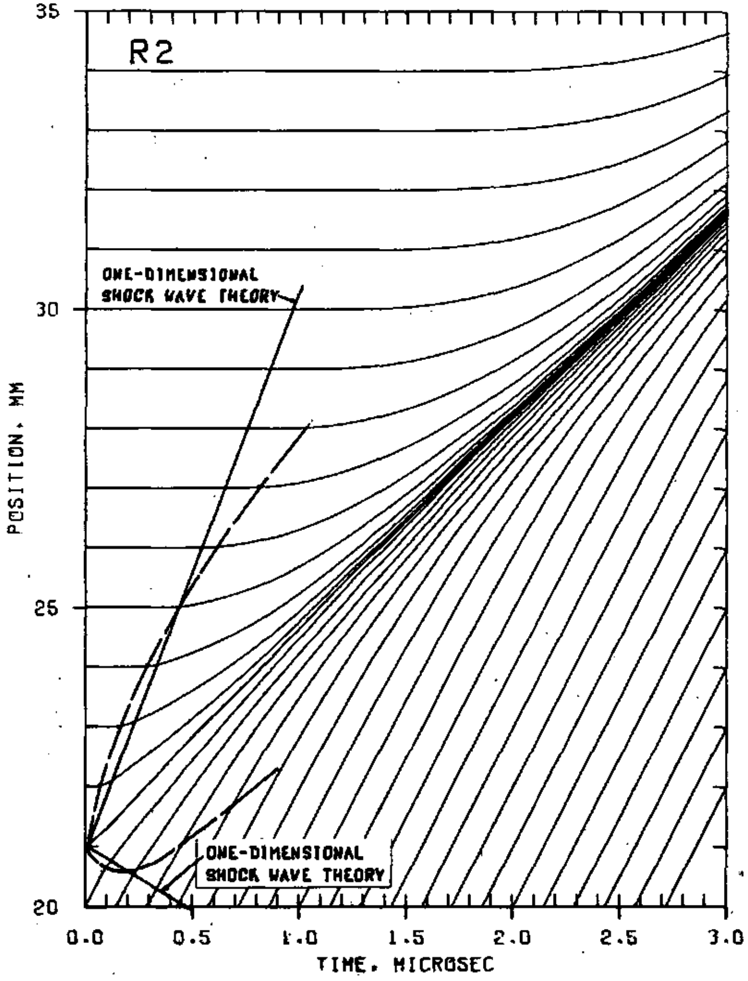

FIGURE 47. POSITION OF TRACERS VS TIME

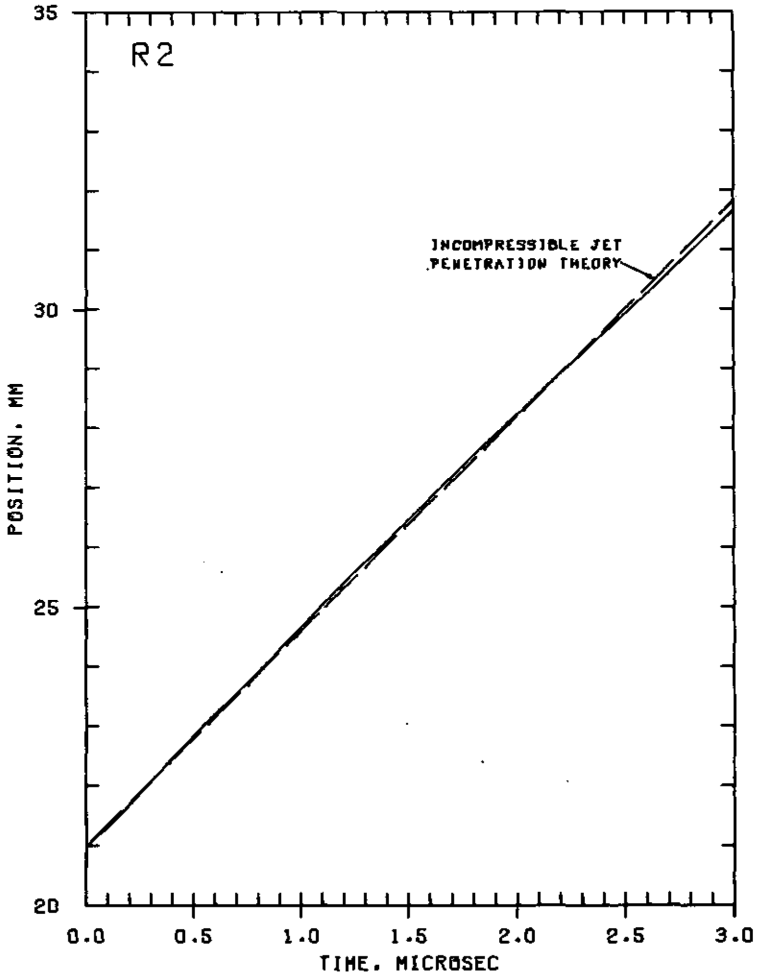

FIGURE 48. POSITION OF INTERFACE VS TIME

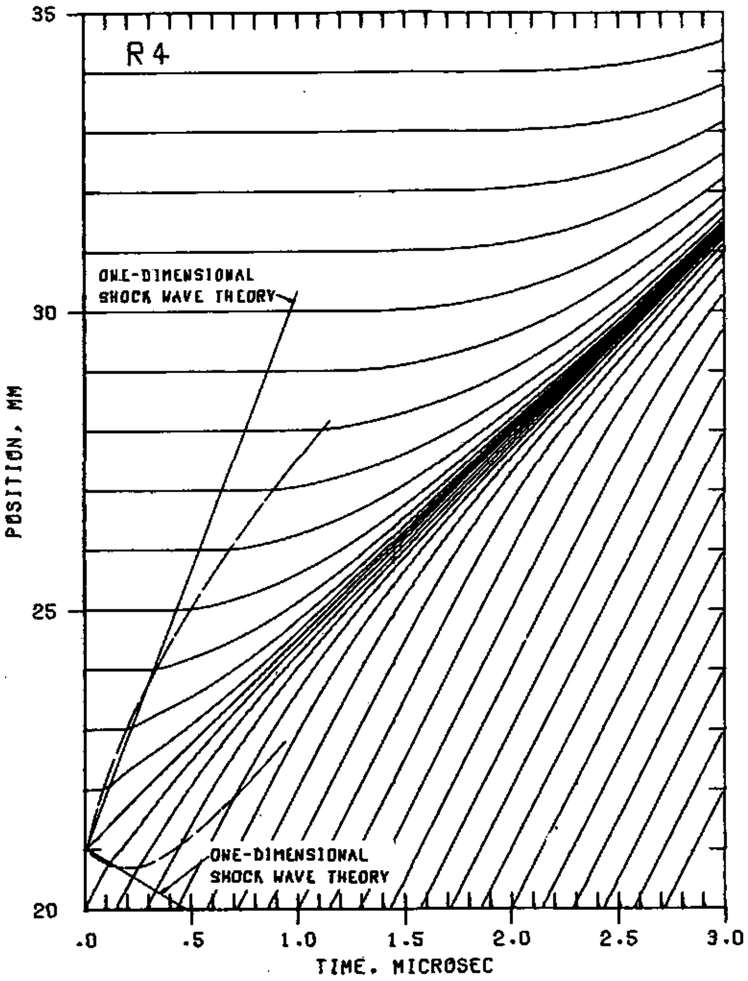

FIGURE 49. POSITION OF TRACERS VS TIME

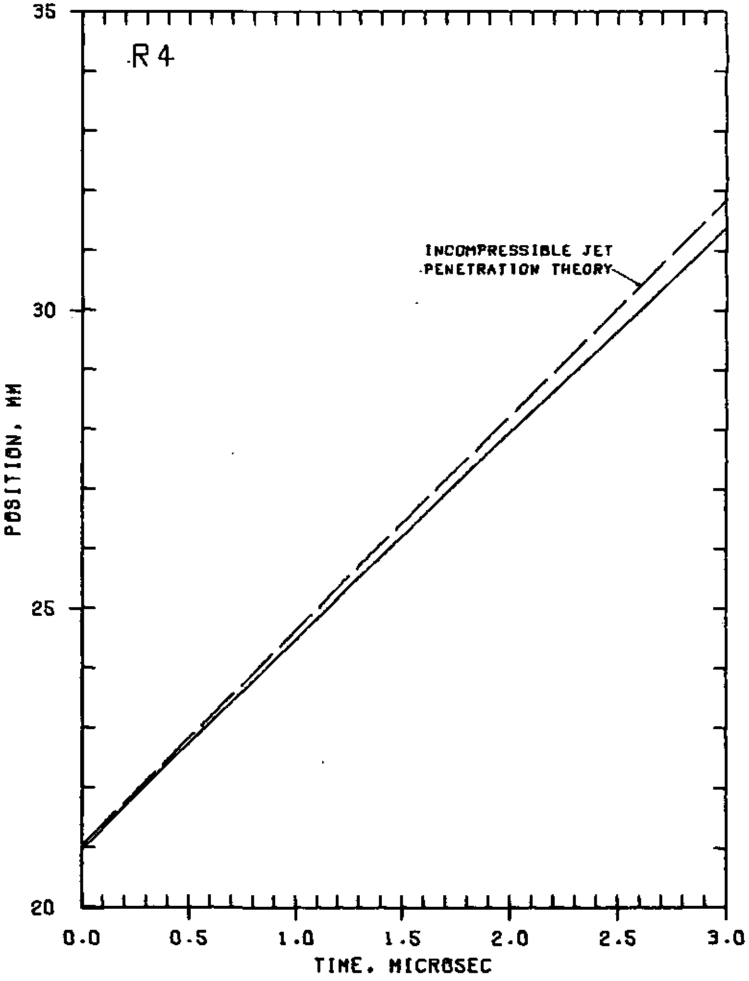

FIGURE 50. POSITION OF INTERFACE VS TIME

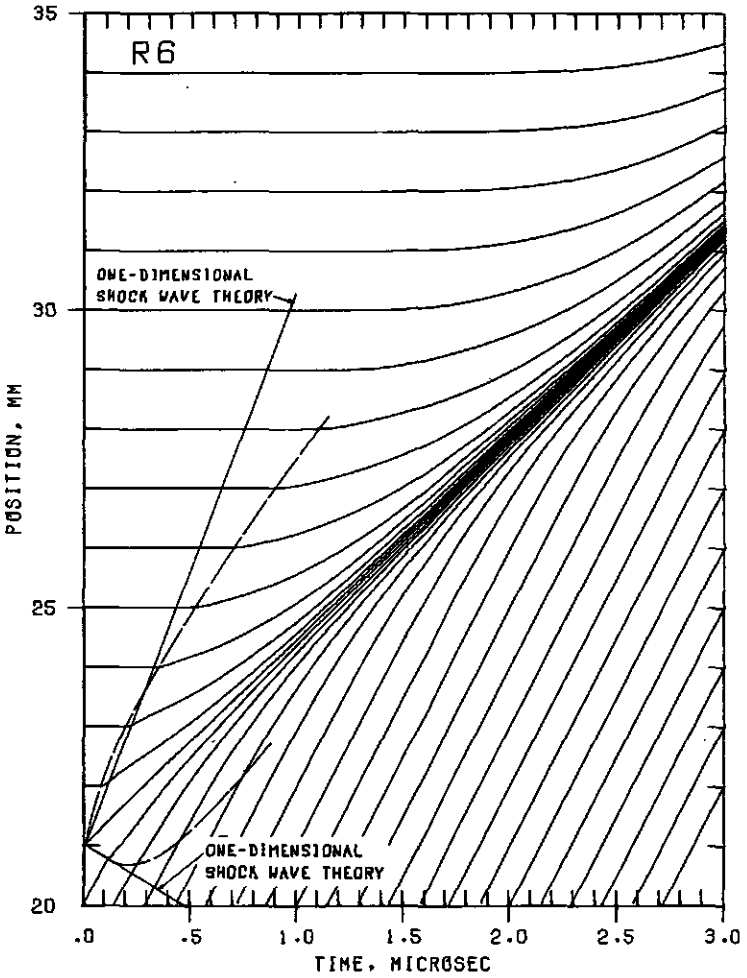

FIGURE 51. POSITION OF TRACERS VS TIME

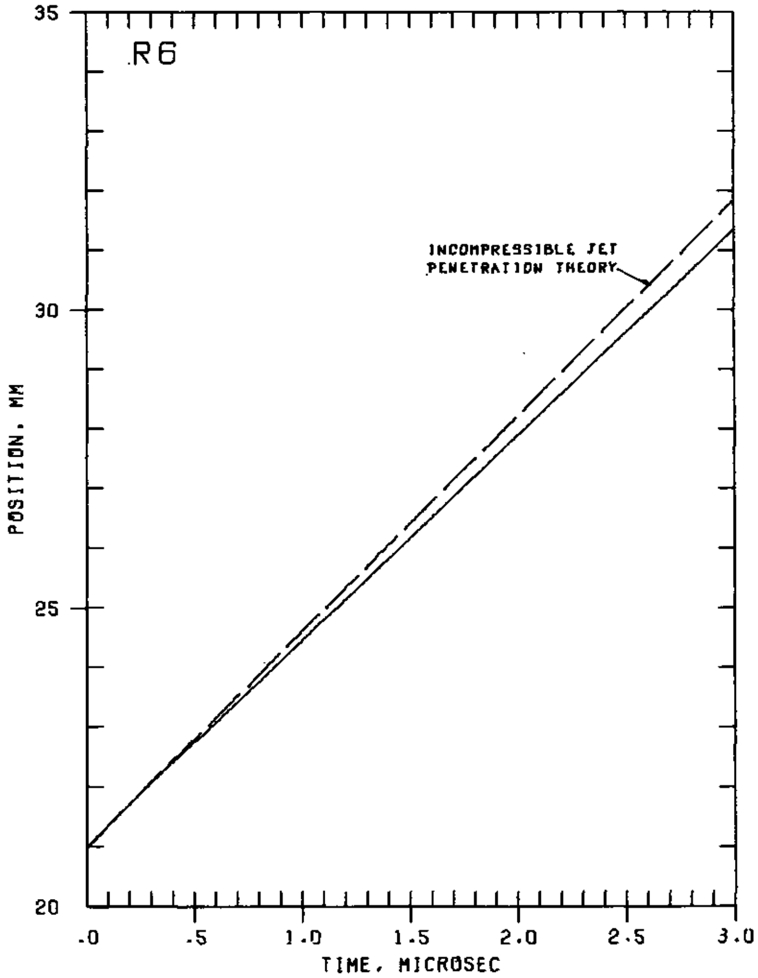

FIGURE 52. POSITION OF INTERFACE VS TIME

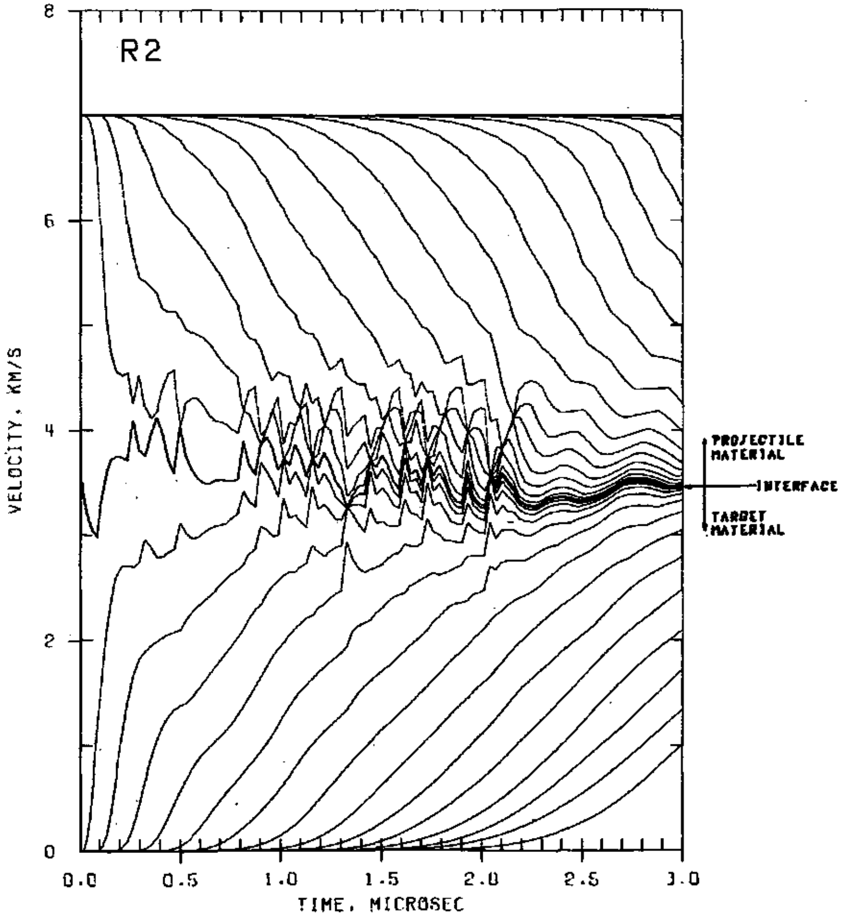

FIGURE 53. VELOCITY OF TRACERS VS TIME

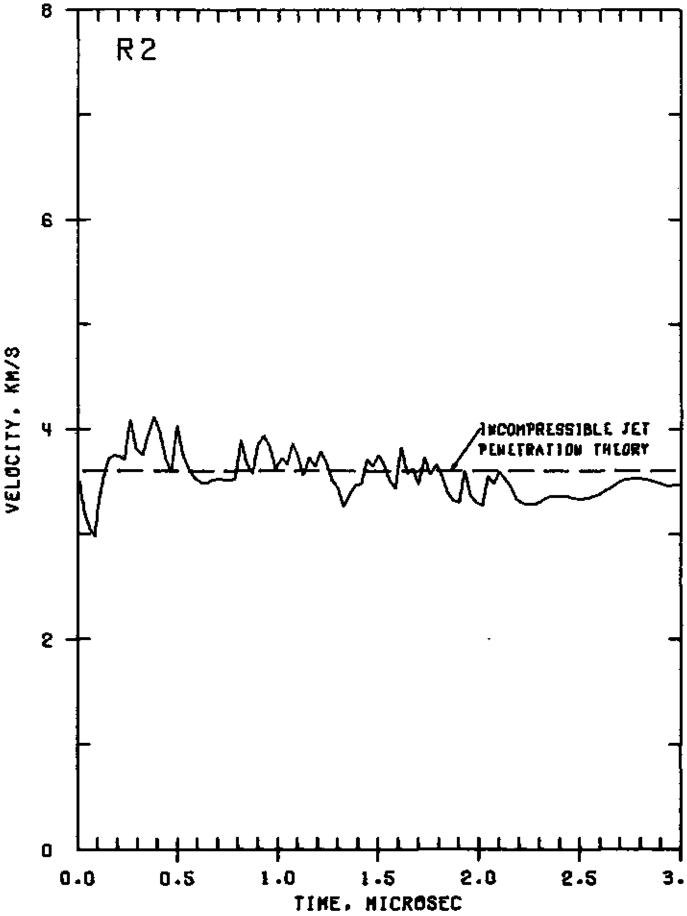

FIGURE 54. VELOCITY OF INTERFACE VS TIME

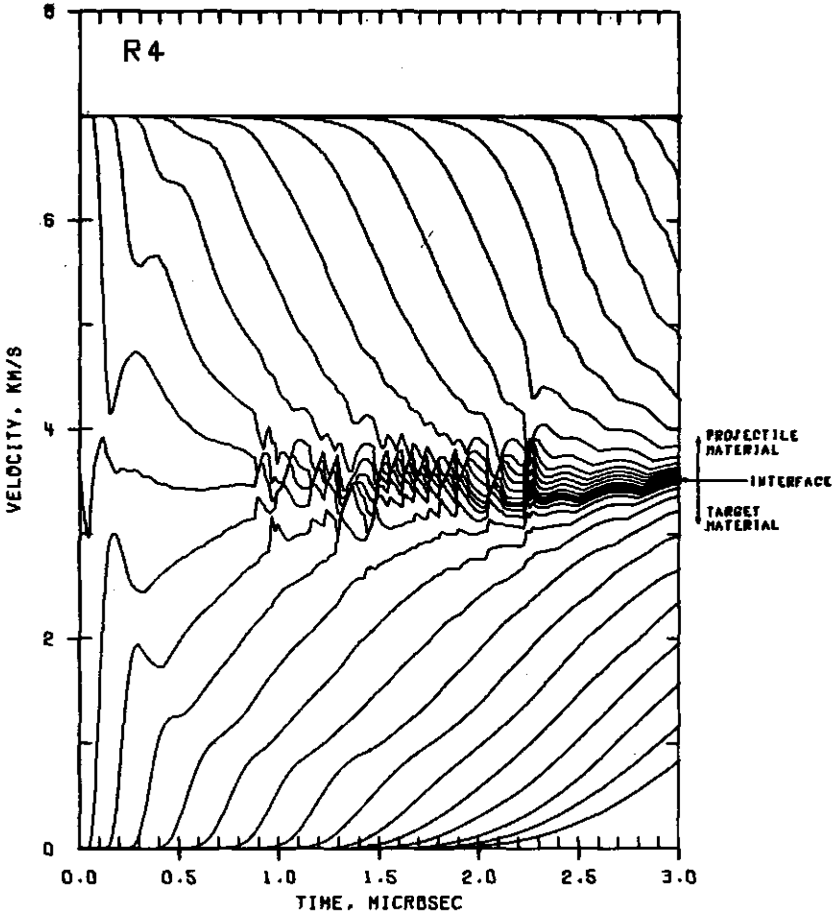

FIGURE 55. VELOCITY OF TRACERS VS TIME

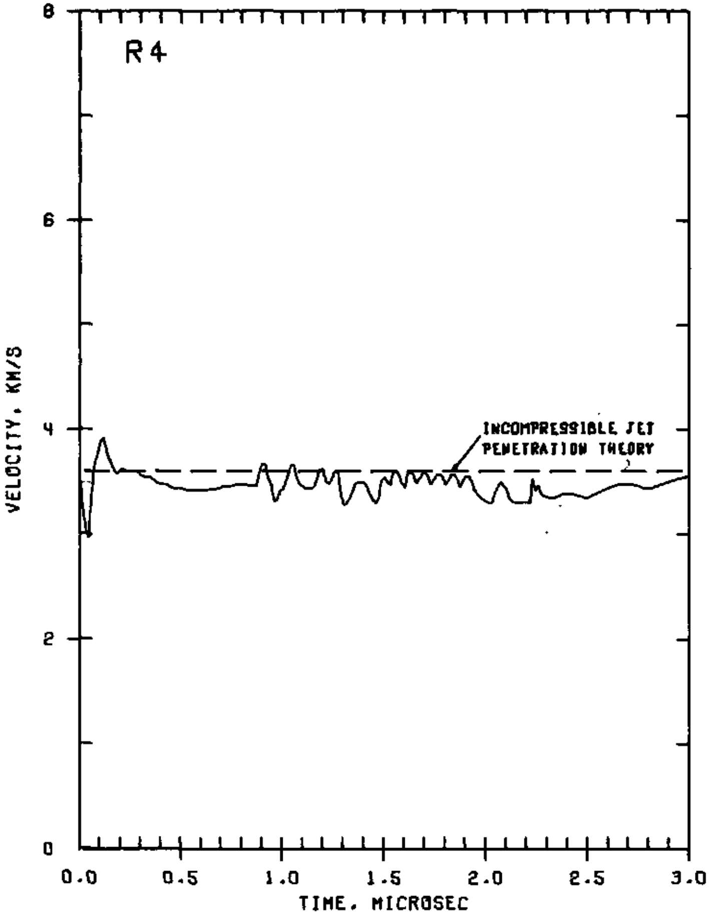

FIGURE 56. VELOCITY OF INTERFACE VS TIME

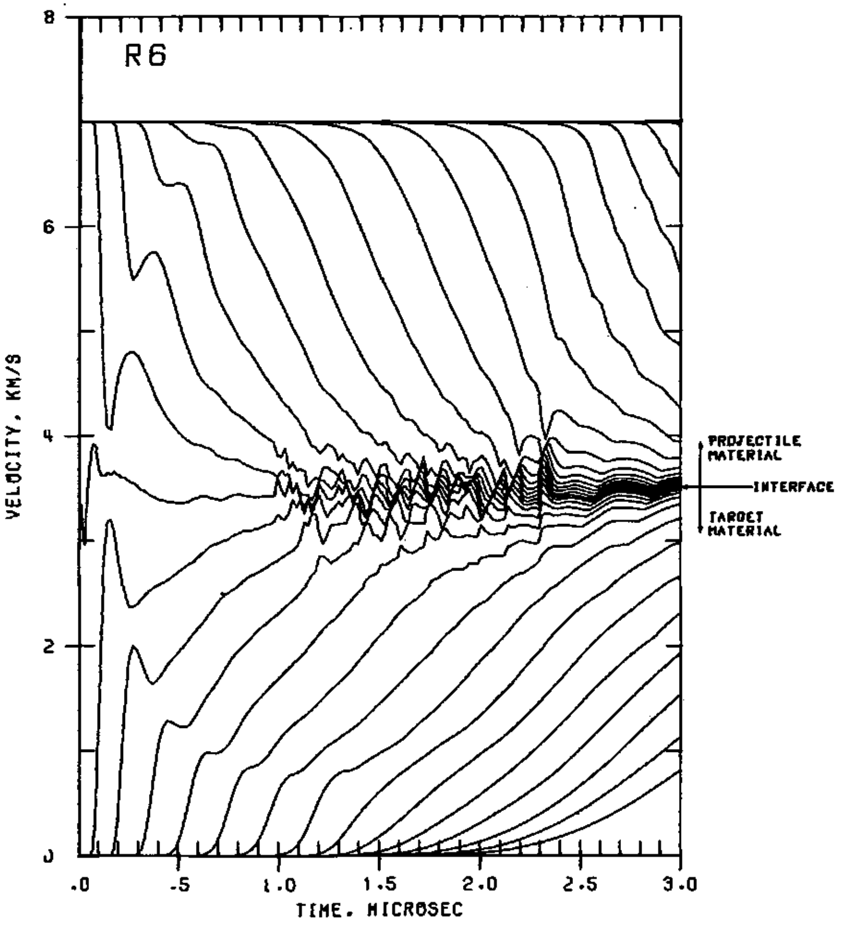

FIGURE 57. VELOCITY OF TRACERS VS TIME

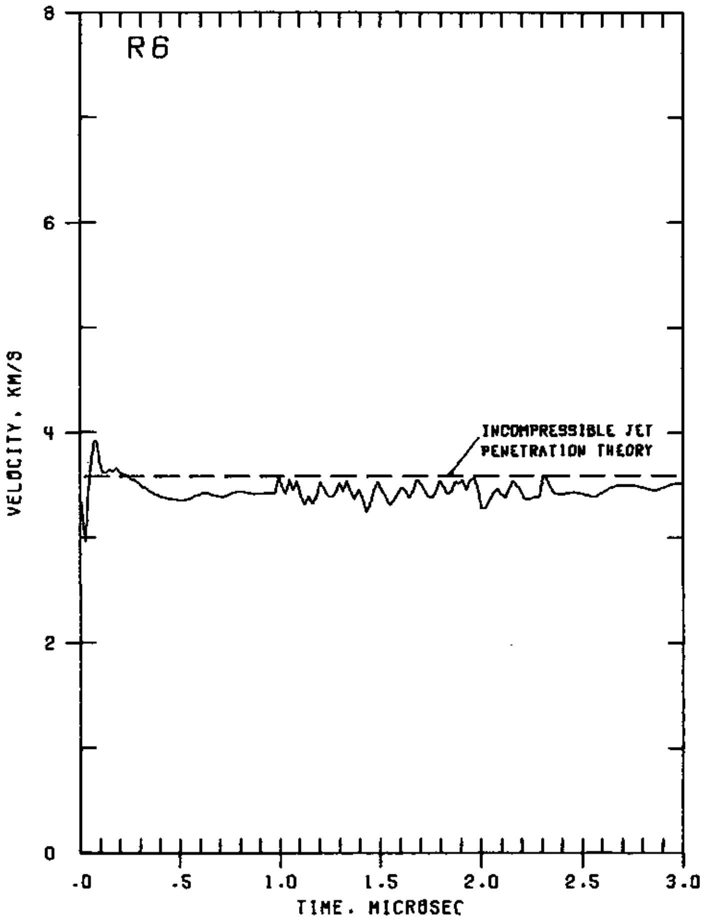

FIGURE 58. VELOCITY OF INTERFACE VS TIME

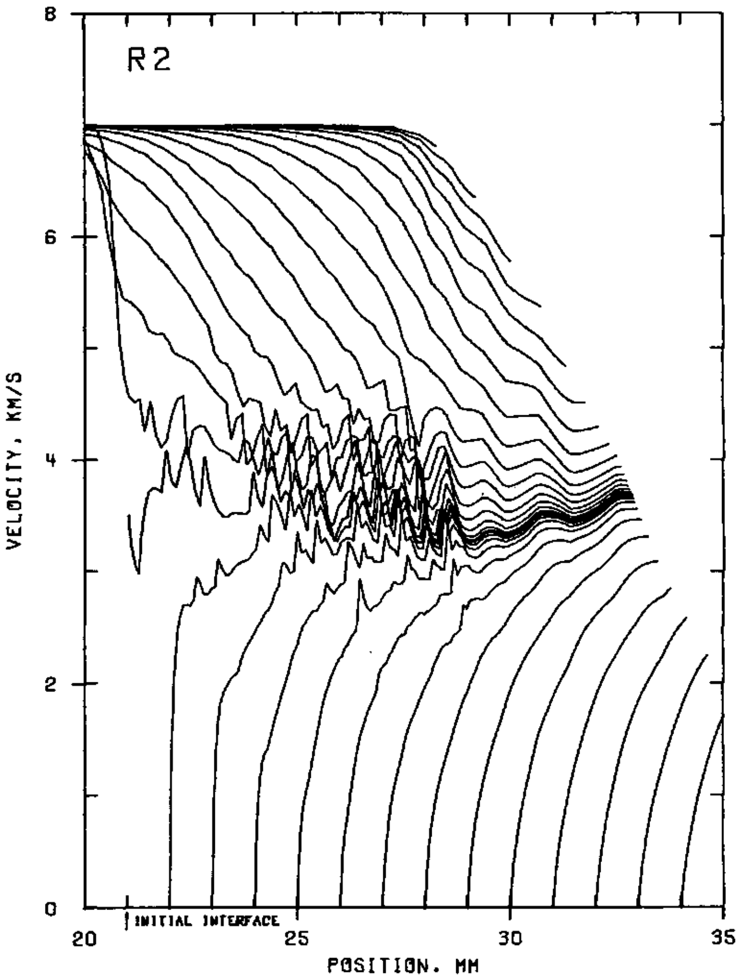

FIGURE 59. VELOCITY OF TRACERS VS POSITION

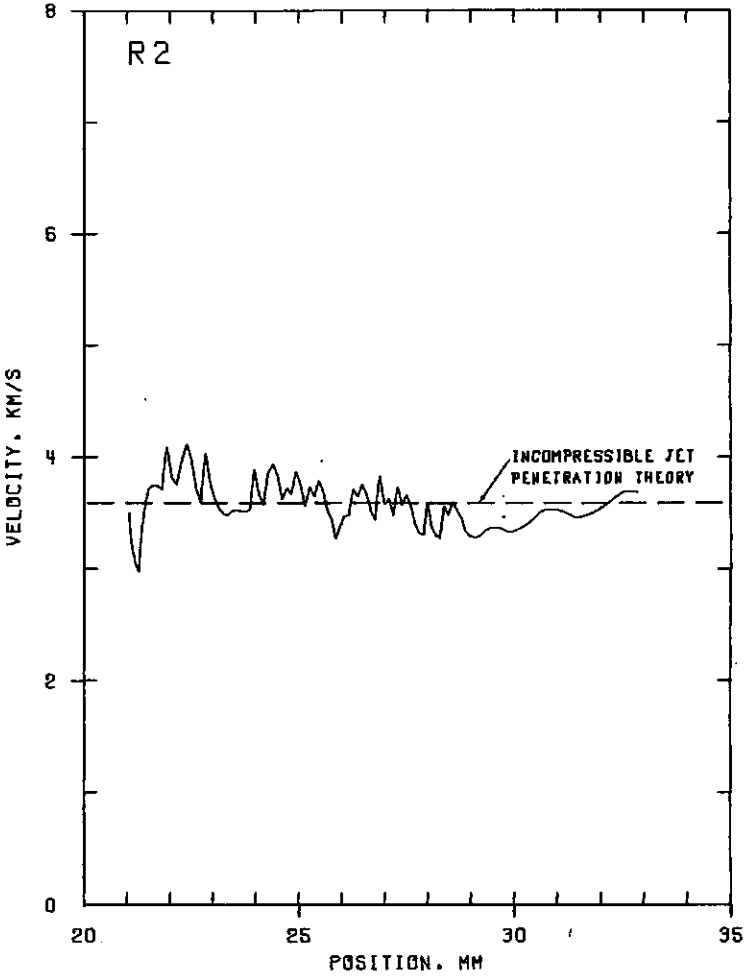

FIGURE 60. VELOCITY OF INTERFACE VS POSITION

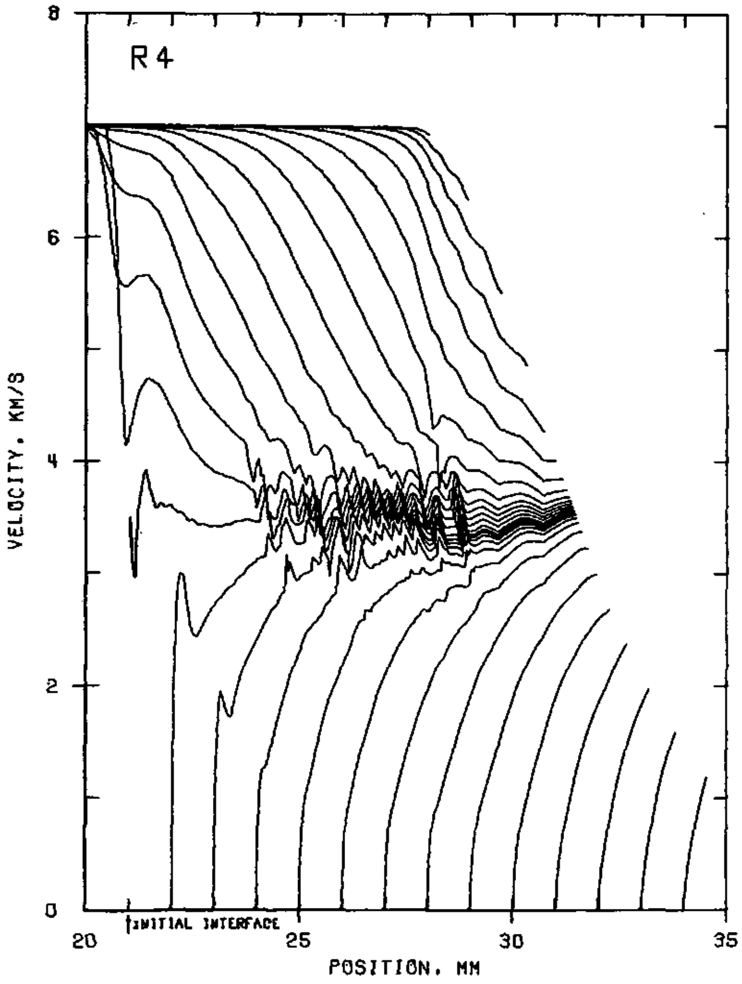

FIGURE 61. VELOCITY OF TRACERS VS POSITION

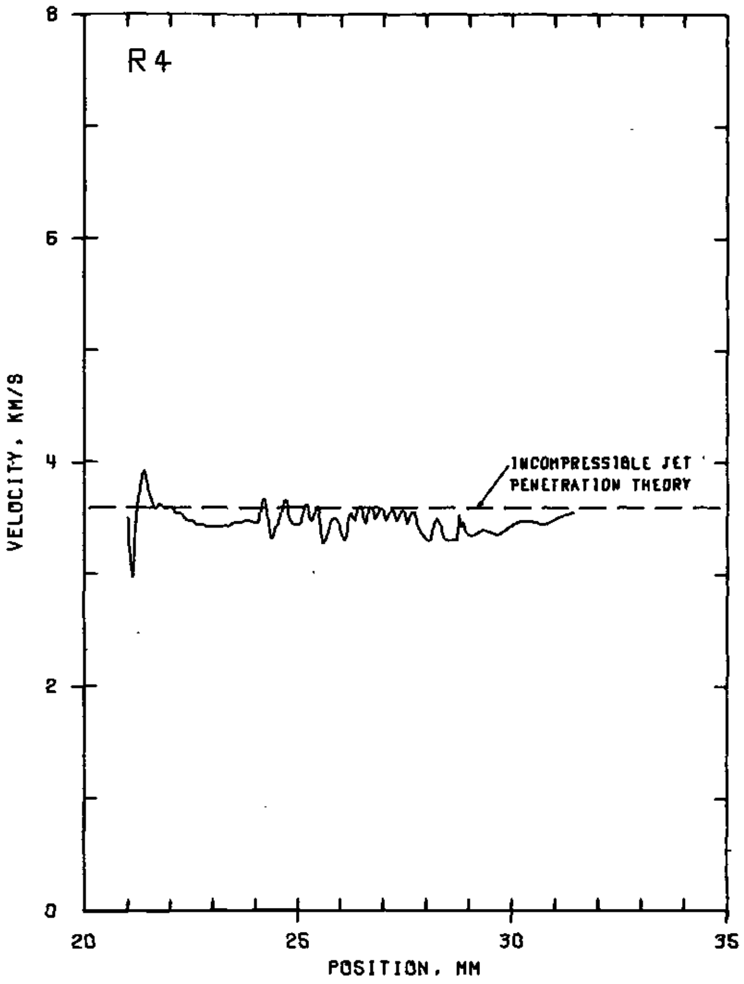

FIGURE 62. VELOCITY OF INTERFACE VS POSITION

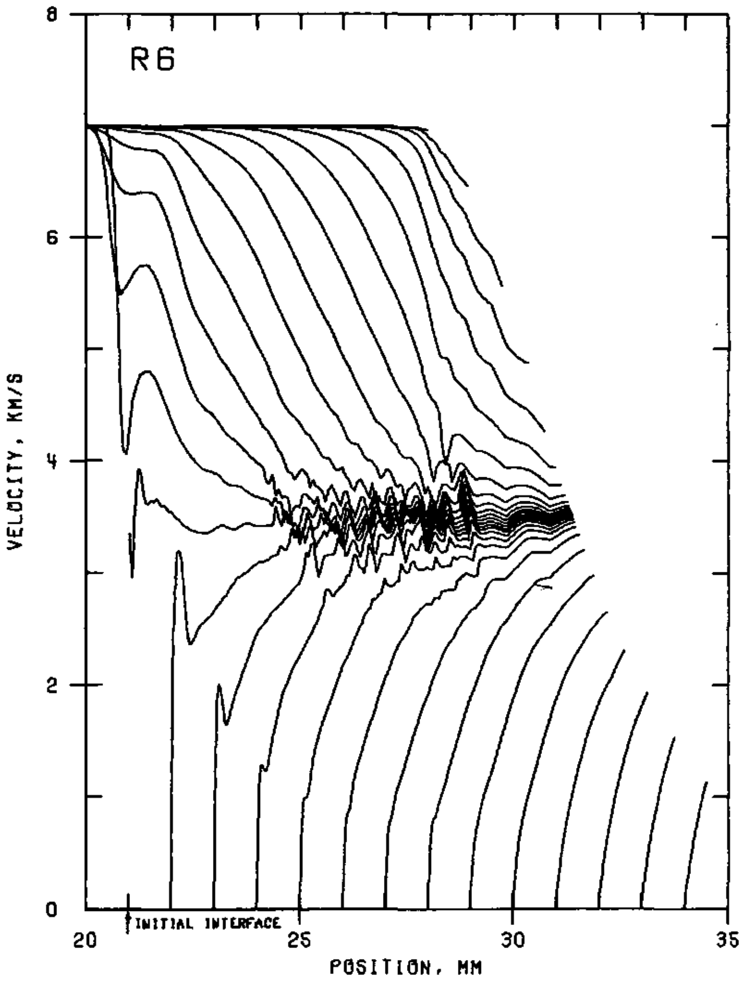

FIGURE 63. VELOCITY OF TRACERS VS POSITION

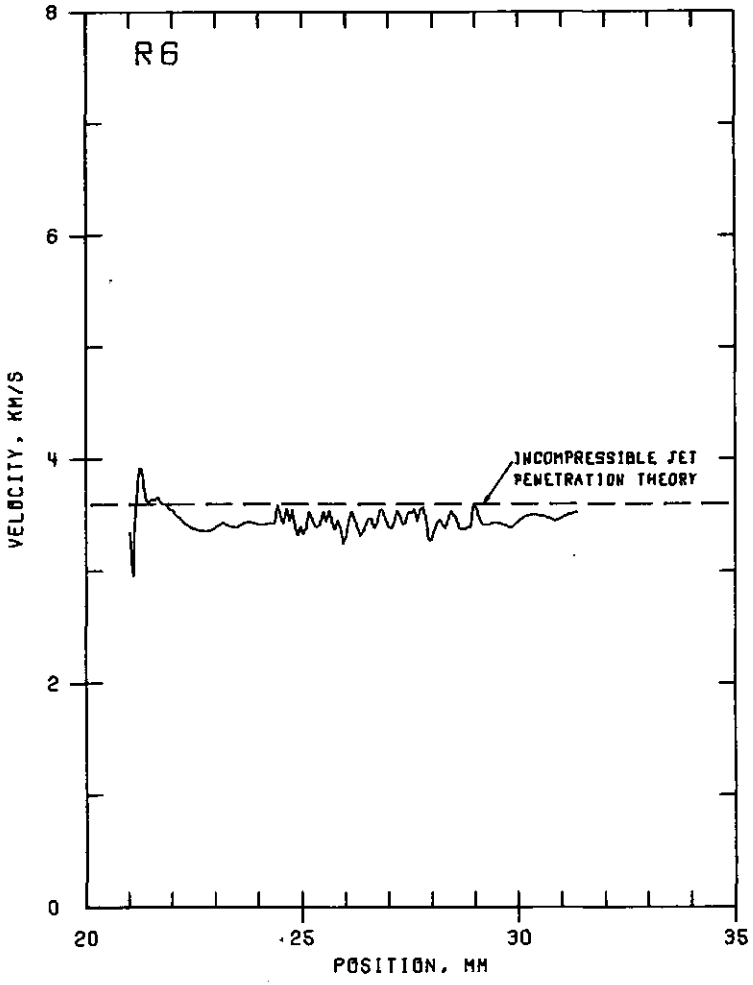

FIGURE 64. VELOCITY OF INTERFACE VS POSITION

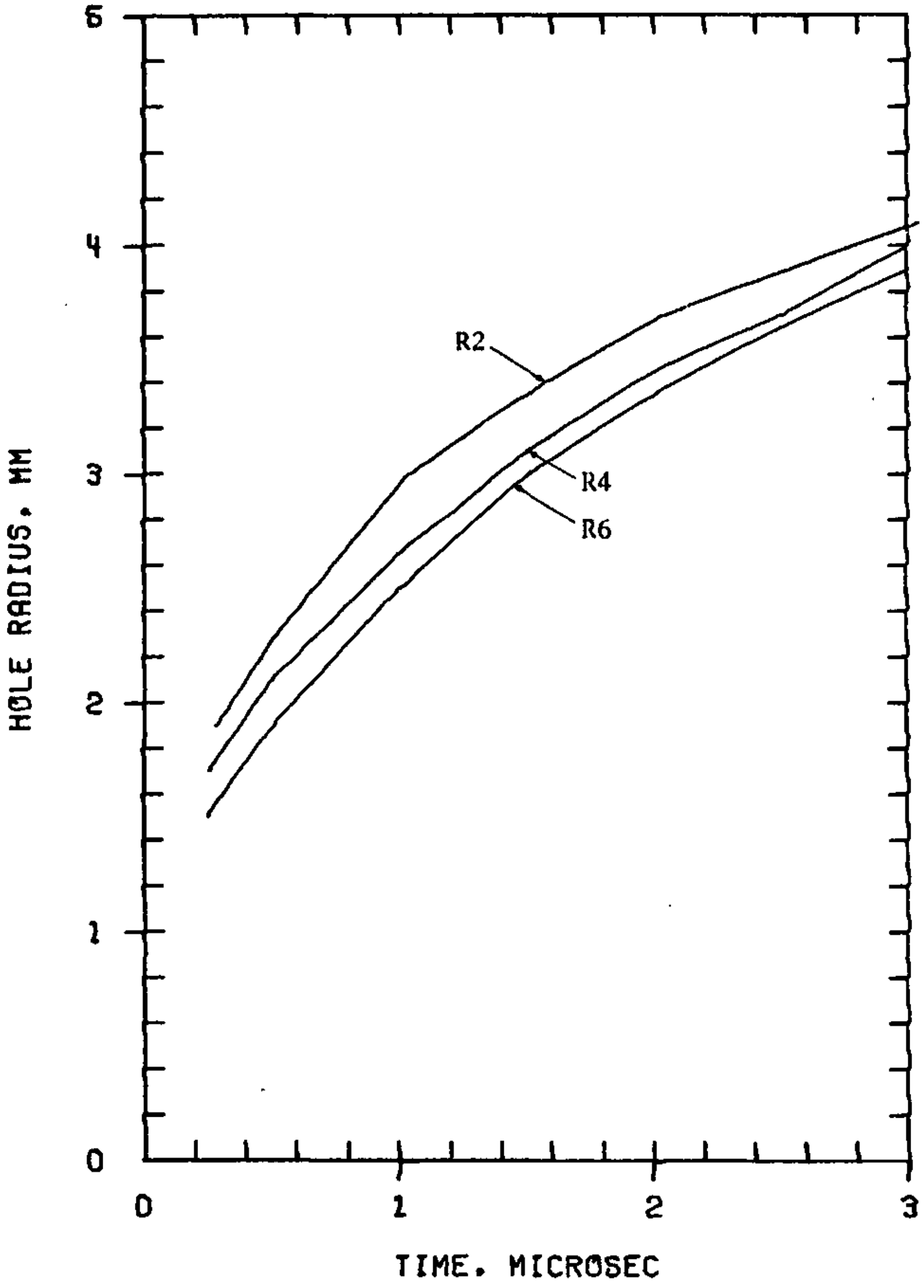

Figure 65. Hole Growth

This page Left Intentionally Blank

DISTRIBUTION LIST

No. of Copies — Organization

12 Commander
Defense Documentation Center
ATTN: DDC-TCA
Cameron Station
Alexandria, VA 22314

1 Director of Defense Research
and Engineering
ATTN: Tech Lib, Rm 3D-1039
Washington, DC 20301

1 Commander
US Army Materiel Development
and Readiness Command
ATTN: DRCDMA-ST
5001 Eisenhower Avenue
Alexandria, VA 22333

1 Commander
US Army Aviation Systems
Command
ATTN: DRSAV-E
12th and Spruce Streets
St. Louis, MO 63166

1 Director
US Army Air Mobility Research
and Development Laboratory
Ames Research Center
Moffett Field, CA 94035

1 Commander
US Army Electronics Command
ATTN: DRSEL-RD
Fort Monmouth, NJ 07703

1 Commander
US Army Missile Command
ATTN: DRSMI-R
Redstone Arsenal, AL 35809

1 Commander
US Army Tank Automotive
Development Command
ATTN: DRDTA-RWL
Warren, MI 48090

No. of Copies — Organization

2 Commander
US Army Mobility Equipment
Research & Development Command
ATTN: Tech Docu Cen, Bldg. 315
DRSME-RZT
Fort Belvoir, VA 22060

1 Commander
US Army Armament Command
Rock Island, IL 61202

2 Commander
US Army Picatinny Arsenal
ATTN: Mr. J. Pearson
Tech Lib
Dover, NJ 07801

1 Commander
US Army Harry Diamond Labs
ATTN: DRXDO-TI
2800 Powder Mill Road
Adelphi, MD 20783

1 Commander
US Army Materials and
Mechanics Research Center
ATTN: Tech Lib
Watertown, MA 02172

1 Director
US Army TRADOC Systems
Analysis Activity
ATTN: ATAA-SA
White Sands Missile Range
NM 88002

1 Assistant Secretary of
the Army (R&D)
ATTN: Asst for Research
Washington, DC 20310

1 Commander
US Army Research Office
P. O. Box 12211
Research Triangle Park, NC 27709

DISTRIBUTION LIST

No. of Copies	Organization
2	Chief of Naval Research Department of the Navy ATTN: Code 427 Code 470 Washington, DC 20325
2	Commander US Naval Air Systems Command ATTN: Code AIR-310 Code AIR-350 Washington, DC 20360
1	Commander US Naval Ordnance Systems Command ATTN: Code ORD-0332 Washington, DC 20360
1	Commander US Naval Surface Weapons Center ATTN: Tech Lib Dahlgren, VA 22448
1	Commander US Naval Surface Weapons Center ATTN: Code 730, Lib Silver Spring, MD 20910
1	Commander US Naval Weapons Center ATTN: Code 45, Tech Lib China Lake, CA 93555
1	Commander US Naval Research Laboratory Washington, DC 20375
1	USAF (AFRDDA) Washington, DC 20330
1	AFSC (SDW) Andrews AFB Washington, DC 20331
1	US Air Force Academy ATTN: Code FJS-RL (NC) Tech Lib Colorado Springs, CO 80840
1	Commander ATTN: Code OOAMA (MMECB) Hill AFB, UT 84401
1	AFWL (SUL) Kirtland AFB, NM 87116
1	AFLC (MMWMC) Wright-Patterson AFB, OH 45433
1	AFAL (AVW) Wright-Patterson AFB, OH 45433
1	Director National Aeronautics and Space Administration Langley Research Center Langley Station Hampton, VA 23365
1	Director Lawrence Radiation Laboratory ATTN: Mr. M. Wilkins P. O. Box 808 Livermore, CA 94550
1	Computer Code Consultants ATTN: W. Johnson 527 Glencrest Drive Solana Beach, CA 92075
1	Physics International Corp ATTN: Dr. C. Godfrey 2700 Merced Street San Leandro, CA 94577
1	Sandia Laboratories ATTN: Dr. L. Bertholf P. O. Box 5800 Albuquerque, NM 87115

DISTRIBUTION LIST

No. of Copies — Organization

1 Systems, Science and Software
ATTN: Dr. R. Sedgwick
P. O. Box 1620
La Jolla, CA 92037

1 Drexel Institute of Technology
Wave Propagation Research Center
ATTN: Prof. P. Chou
32nd & Chestnut Streets
Philadelphia, PA 19104

2 University of California
Los Alamos Scientific Lab
ATTN: Mr. J. M. Walsh
Tech Lib
P. O. Box 1663
Los Alamos, NM 87545

Aberdeen Proving Ground

Marine Corps Ln Ofc
Dir, USAMSAA